EarthArXiv Coversheet

Title: Meteorological Drivers of Resource Adequacy Failures in Current and High Renewable Western U.S. Power Systems

Authors:
Srihari Sundar
sriharis@umich.edu, Twitter: @srisun14
Department of Aerospace Engineering, University of Michigan, Ann Arbor, Michigan, USA

Michael T. Craig
mtcraig@umich.edu, Twitter: @TheEnergyCraig
School for Environment and Sustainability, University of Michigan, Ann Arbor, Michigan, USA

Ashley Payne
Tomorrow.io, Boston, MA, USA

David J. Brayshaw
Department of Meteorology, University of Reading, Reading, UK

Flavio Lehner
Department of Earth and Atmospheric Sciences, Cornell University, Ithaca, NY, USA
Climate and Global Dynamics Laboratory, National Center for Atmospheric Research, Boulder, CO, USA

This preprint is under review at *Nature Communications* and is not peer reviewed.

Meteorological Drivers of Resource Adequacy Failures in Current and High Renewable Western U.S. Power Systems

Srihari Sundar[1*], Michael T. Craig[2,3*], Ashley Payne[4], David J. Brayshaw[5] and Flavio Lehner[6,7,8]

[1,*]Department of Aerospace Engineering, University of Michigan, Ann Arbor, Michigan, USA.
[2,*]School for Environment and Sustainability, University of Michigan, Ann Arbor, Michigan, USA.
[3]Department of Industrial and Operations Engineering, University of Michigan, Ann Arbor, Michigan, USA.
[4]Tomorrow.io, Boston, MA, USA.
[5]Department of Meteorology, University of Reading, Reading, UK.
[6]Department of Earth and Atmospheric Sciences, Cornell University, Ithaca, NY, USA.
[7]Climate and Global Dynamics Laboratory, National Center for Atmospheric Research, Boulder, CO, USA.
[8]Polar Bears International, Bozeman, MT, USA.

*Corresponding author(s). E-mail(s): sriharis@umich.edu; mtcraig@umich.edu;

Abstract

Power system resource adequacy (RA), or its ability to continually balance energy supply and demand, underpins human and economic health. How meteorology affects RA and RA failures, particularly with increasing penetrations of renewables, is poorly understood. We characterize large-scale circulation patterns that drive RA failures in the Western U.S. at increasing wind and solar penetrations by integrating power system and synoptic meteorology methods. At up to 60% renewable penetration and across analyzed weather years, three high pressure patterns drive nearly all RA failures. The highest pressure anomaly is the dominant driver, accounting for 20-100% of risk hours and 43-100% of cumulative risk at 60% renewable penetration. The three high pressure patterns exhibit positive surface temperature anomalies, mixed surface solar radiation anomalies, and negative wind speed anomalies across our region, which collectively increase demand and decrease supply. Our characterized meteorological drivers align with meteorology during the California 2020 rolling blackouts, indicating continued vulnerability of power systems to these impactful weather patterns as renewables grow.

Keywords: power system resource adequacy, power system reliability, large-scale circulation patterns, meteorological drivers, Western Electricity Coordinating Council, capacity expansion, self-organizing maps

1 Introduction

Access to reliable, or uninterrupted, and low-cost electricity underpins human health, and well-being [1]. Designing a reliable system while minimizing costs is the central objective of power system planning [2]. Reliability partly depends on maintaining resource adequacy (RA), which is the system's ability to continually balance electricity supply (or generation) and demand despite the occurrence of unexpected events [3]. RA failures, i.e., times where demand exceeds supply operationally at bulk power systems (BPS) level, are often responsible for large-scale rolling outages, e.g. in California in 2020 [4] and Texas [5] in 2021. These two events were caused by a combination of higher than anticipated demand, due to a heatwave (in CA) and a cold snap (in TX), and generator outages driven by extreme weather. This necessitated intervention, like rolling outages, from the system operator to prevent catastrophic consequences to the system.

Meteorology affects RA through effects on electricity supply and demand. In BPS dominated by thermal electricity generators, surface air temperature is the main meteorological driver of supply and demand. Low and high surface air temperatures affect demand through increased use of building heating, ventilation, and air conditioning (HVAC) for heating and cooling, respectively [6, 7]. Surface air temperature also affects supply. Specifically, extreme heat increases deratings of thermal power plants [8, 9] and solar photovoltaics, while extreme cold and heat increases forced outage rates of thermal and hydroelectric power plants [10].

Two trends complicate the link between meteorology and RA: (1) increasing penetrations of wind and solar power, and (2) non-stationary meteorology driven by natural variability and anthropogenic climate change. Since wind and solar power are a function of wind speeds and solar irradiance, increasing wind and solar power penetrations will increasingly link electricity supply to these meteorological variables. Wind speeds and solar irradiance exhibit significant spatio-temporal variability [11, 12] and forecast and projection uncertainty [13, 14], complicating RA assessment. Non-stationary meteorology driven by intensifying climate change further complicates RA assessment. As historical meteorology becomes increasingly non-representative of future meteorology, RA assessment of future system fleets will need to increasingly rely on projected future meteorological timeseries to account for the transient nature of the current climate state. However, generating high-quality meteorological projections that account for climate change remains an active area of research limited by methodological uncertainties, and computational power [15]. Generating high-quality future meteorological timeseries is especially challenging at the high spatio-temporal resolution (e.g., hourly) typically required for RA analyses [16].

In response to these challenges, this paper aims to better understand the meteorological drivers of RA, focusing specifically on RA failures, and how increasing renewable generation affects those drivers. Better understanding these relationships is crucial for several reasons. First, the meteorology that drives (and co-occurs with) RA failures will determine human health impacts, which can be highly heterogeneous across space and socioeconomic groups [17]. Better understanding the link between decarbonization and drivers of RA failures can shed light on investment needs in BPS and communities to mitigate possible health impacts and achieve more equitable outcomes. Second, characterization of historic meteorological drivers can guide in evaluating, selecting, and downscaling general circulation models, which is essential for making informed adaptation investments in the power sector [18, 19]. Third, once meteorological drivers of RA failures are characterized, long-range probabilistic forecasting at the subseasonal to seasonal scale can act as a more informed early warning system for system operators and emergency preparedness organizations [20].

We characterize meteorological drivers of RA failures using weather regimes. Weather regimes represent atmospheric circulation as belonging to a finite number of states or patterns [21, 22]. These states are constructed by applying clustering techniques to variables representing large-scale atmospheric flows, e.g., geopotential height. The resulting large-scale patterns have strong associations with surface-level meteorological variables that directly affect the power system, including extreme surface air temperatures [23–25]. These patterns indicate several processes like temperature advection and subsidence which can, under certain conditions, drive extreme events in the power system. The patterns persist over large spatial and temporal scales, and unlike the high-frequency variations exhibited by surface meteorology, the patterns' spatio-temporal variations are better captured by general circulation models (GCMs). Previous research has sought to link the changes in frequency and return periods of these large-scale patterns with the occurrence of extreme events under a changing climate using data from GCMs [26–29]. The spatial coverage of these large-scale atmospheric circulation patterns makes them valuable analogues for surface meteorology over large geographic regions. Using these synoptic drivers in planning and operations can benefit system operators when thinking about RA due to current and future systems' increasing dependence on generation over larger areas and interconnected balancing authorities.

Our research contributes to two literatures. The first literature analyzes meteorological drivers in the power system, but does not consider RA, a gap that we fill. Within this set, a few studies examine meteorological drivers of periods of low renewable generation or high net demand (demand minus renewable generation) [30–33]. Meteorological drivers in these papers include surface meteorology and atmospheric circulation during these periods. Further, other studies describe weather regimes as drivers of renewable generation, variability, and net demand in the European power system [34–36]. The second literature analyzes RA, but does not consider meteorological drivers, a gap that we also fill. In this broad RA umbrella, studies quantify the effect of using different RA metrics on reserve procurement decisions [37] and capacity values [38]. Other studies quantify the contribution of generators [39, 40] and transmission [41] to RA. A final group of studies quantify system RA under changing generator and/or weather. For instance, Turner et. al. [42] quantify RA changes (in probability and magnitude) driven by decarbonization decisions and climate change impacts on electricity demand and hydropower generation in the Pacific Northwest.

To address these gaps, we answer the following research questions: What large-scale circulation patterns drive risk of regional resource adequacy failures? And how do these drivers change with increasing wind and solar penetrations? We define resource adequacy (RA) as the ability of a power system to continually balance electricity supply and demand [3], and quantify RA on a probabilistic, hour-to-hour operational basis. We conduct our study for the U.S. Western Electricity Coordinating Council (WECC) footprint given its rapid growth in wind and solar penetrations, aggressive wind and solar targets, and recent resource adequacy failure [43]. Using a one-way impact analysis that decides fleet investment to meet the standard resource adequacy target (1 day in 10 years), identifies resource adequacy failures, and finds meteorological drivers of these failures for increasing renewables penetrations, our research is the first to link weather patterns and power systems operations in the United States, and the first to characterize weather regimes driving RA failures.

Our analytical pipeline uses methods from power system and synoptic meteorology domains [Figure 1]. We first construct fleets that generate increasing levels of wind and solar electricity (hereafter renewable electricity or RE) using a capacity expansion model (CEM) (see Methods.4.2). The CEM is a deterministic linear program that minimizes total system cost, which is the sum of the cost of new capacity investments and the cost of electricity generation of existing and new units. The cost of electricity generation is the sum of fixed operations and maintenance (O&M) costs and variable electricity generation costs, which include fuel costs and variable O&M costs. The CEM specifically optimizes new investments in wind, solar, 4-hour electricity storage facilities, inter-regional transmission capacities, and operations of existing and new units, and inter-regional electricity flows. The CEM does not optimize investment in new thermal facilities given its coupling with our RAM, which adds or removes thermal facilities to reach a given reliability target. Investment and operational decisions are subject to numerous generator- and system-level constraints, including hourly balance of supply and demand and electricity flows, limited inter-regional electricity flows, hourly site-specific wind and solar resource availability, engineering and economic-based unit operations, and limited technology-specific investments. To capture co-variability and extremes in electricity demand and wind and solar generation, we use observed hourly electricity demand for WECC [44] and coincident spatially-differentiated RE capacity factors (see Methods.4.5). In our models we divide WECC into five constituent sub-regions, as used by WECC in its Western Assessment of Resource Adequacy report (ref SI fig. A.3) [45]. Between each pair of sub-regions, we model transmission flows using the transport method, which caps hourly inter-regional electricity flows between sub-regions to a fixed transmission capacity. Investment decisions in storage, occur at the five-region level; in transmission, between each pair of regions; and in wind and solar, at spatially-differentiated resource locations on a roughly 30 by 30 km grid. RE penetration levels are enforced at the WECC scale.

We then quantify a RA profile for each fleet and each sub-region from the CEM using a resource adequacy model (RAM), which simulates stochastic forced outages of generators using a non-sequential Monte Carlo sampling procedure and finds hours where there is a non-zero probability of demand exceeding total available generation (see Methods.4.3). We use empirically-derived temperature-dependent forced outage rates for NGCC and hydropower facilities, constant outage rates for other generators, and do not account for outages in storage units [10, 46]. Storage assets are dispatched on a chronological hourly basis within the RA model within each Monte Carlo iteration after dispatching all the other generators using a greedy dispatch policy [39, 47]. From the RAM, we obtain a timeseries of loss of load probabilities (LOLPs) by hour of the year, which we refer to as the RA profile. This RA profile is a function of short-term operations from the RAM. Hours with LOLPs greater than zero indicate a risk of an RA failure; we refer to these hours as RA risk hours or risk hours.

Finally, to characterize the meteorological drivers of RA failure, we map the 500hPa geopotential height (Z500) anomalies in these risk hours to the western US summer weather regimes. These regimes are constructed based on June - September daily Z500 anomalies from a 40 year period using self organizing maps (SOM), and each regime is represented by a characteristic weather pattern (WP) (see Methods.4.4). The characteristic WPs show regimes with varying Z500 anomalies over the region, ranging from positive anomalies (high pressure systems, WP7) to negative anomalies (low pressure systems, WP3) [Figure 1 Weather Regimes panel]. Each weather regime produces different surface weather patterns, e.g. high pressure anomalies in WPs 7 and 8 drive extreme heat events across the Western US, as later illustrated in our results.

The WPs corresponding to regimes identified based on the risk hours characterize the large-scale patterns contributing to RA failures. By running this integrated modeling framework for four weather years (2016 through 2019) and RE penetrations (Current, 30%, 45%, and 60%, see sec. 4.6 for definition of RE penetration), we quantify the effect of increasing renewables on meteorological drivers of RA and the robustness of this effect across independent weather years. While using four weather years does not sample the full distribution of possible weather events and associated impacts on RA and RA failures, it does cover over 35,000 hours and permits us to use observed hourly electricity demand with coincidental wind and solar generation.

Using this analytical pipeline, in this work, we show that RA failures in WECC are driven by WPs corresponding to high pressure anomalies (WPs 6, 7, and 8 in Figure 1) over the region. These WPs correspond to high surface air temperatures and low wind speeds across WECC and with low solar irradiance in large areas with solar PV facilities. These meteorological conditions cause compounding impacts on electricity supply and demand, ultimately resulting in risk of resource inadequacy (i.e., RA failures). As renewable penetrations increase, the risk of RA failures increasingly concentrates within the WP with the highest pressure anomaly (WP 7).

2 Results

We divide our results into two sections. First, we quantify the effect of increasing renewable penetrations on meteorological drivers of risk hours for a single weather year (2019). Second, we repeat this analysis to characterize meteorological drivers of risk hours across multiple weather years at increasing renewable penetrations. We restrict our analysis to the CAMX region for two reasons. First, NERC's Long-Term Reliability Assessment (LTRA) indicates CAMX is the most vulnerable WECC region to resource adequacy failures in the near term, with LOLH of 0.72 and 9.79 in 2024 and 2026 respectively in the 2022 assessment. By comparison, other regions in WECC have LOLH of up to 0.03 (2024) and 0.37 (2026), an order of magnitude less than CAMX. Thus, understanding meteorological drivers of RA failures in CAMX can provide significant near-term value to decision makers and serve as a model for analyses in future regions. Our resource adequacy results agree with the LTRA, as we find CAMX has at least 4x and 27x more probability of resource adequacy failure than any other WECC region in the current and RE penetration greater than 30% fleets respectively across the years. Second, we find that in all but one scenario we analyze, and in all RE penetration greater than or equal to 30%, the CAMX risk hours coincide with risk hours in other regions if failures occur in other regions. Across the weather years, the current fleets correspond to a RE penetration ranging from 9% - 9.4%, so we denote these fleets as 9 % RE penetration in our results.

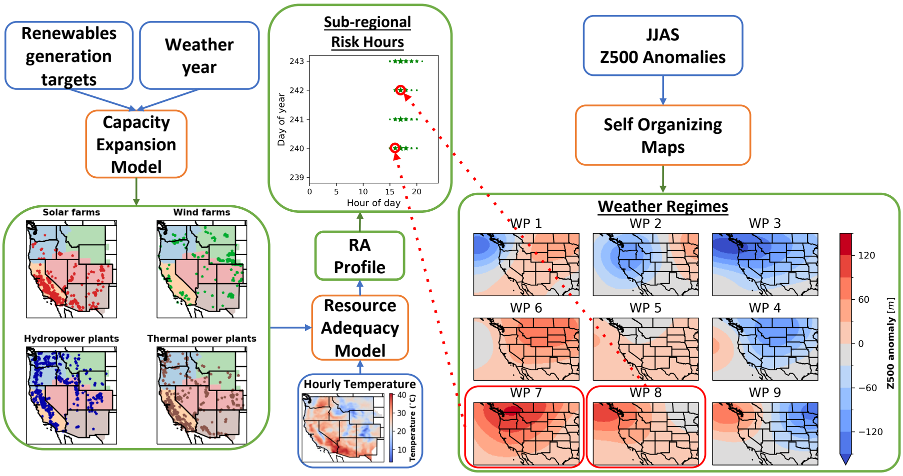

Fig. 1: **Analytical pipeline** We use a capacity expansion model (CEM) to construct generator fleets with increasing renewable penetrations and different weather years. Maps show the sizes and locations of facilities for 60% renewables penetration and 2019 weather. These fleets are input into a resource adequacy model (RAM) to quantify hourly loss of load profiles (LOLPs), yielding a resource adequacy (RA) profile (in this figure we only represent the RA risk hours). We then map the risk hours in the RA profile to weather regimes, which we identify with self-organizing maps (SOMs) applied to 500hPa geopotential height (Z500) anomalies. Depicted weather regimes are the SOM outputs for extended summer months, with positive anomalies (high pressure systems) in the bottom left and negative anomalies (low pressure systems) in the top right. By varying renewable penetrations and weather years, we characterize meteorological drivers of risk hours. Red arrows depicting attribution of risk hours to weather regimes is for illustrative purposes only.

2.1 Meteorological drivers under increasing renewable penetrations for the 2019 weather year

Using our CEM, we construct generator fleets in which RE generation accounts for increasing percentages of annual demand. As renewable penetrations increase from 9% (or current levels) to 60% of annual demand, wind, solar, and storage capacities (at the interconnection level) increase from 20 GW, 16 GW, 5 GW to 103 GW, 70 GW, and 7 GW respectively, while NGCC capacities decrease from 49 GW to 35 GW [Figure 2, see SI fig. A.8 for subregional regional capacities]. Figure 3 depicts each system's RA profile by showing the magnitude of hourly LOLP and timing of risk hours. Across renewable penetrations, all risk hours occur in the extended summer months (i.e., June through September or JJAS). Most risk hours occur between 4 and 8 PM Pacific Standard Time (PST). As renewable penetrations increase from 9% to 60%, the number of risk hours decrease from 68 to 10 and increasingly concentrate into the period between 6 and 8 PM PST. The decrease in risk hours is driven by increasing available generation in many hours of the year, including in hours that previously had low LOLPs. In these hours, increasing available generation results from wind and solar capacity increases exceeding NGCC capacity decreases. Particularly, the increasing storage capacity reduces risk in the early evenings. As risk hours decrease, hourly LOLPs increase. For instance, as renewable penetrations increase from 9% to 60%, maximum LOLPs increase from 0.27 to 0.63 [SI fig. A.9(b)].

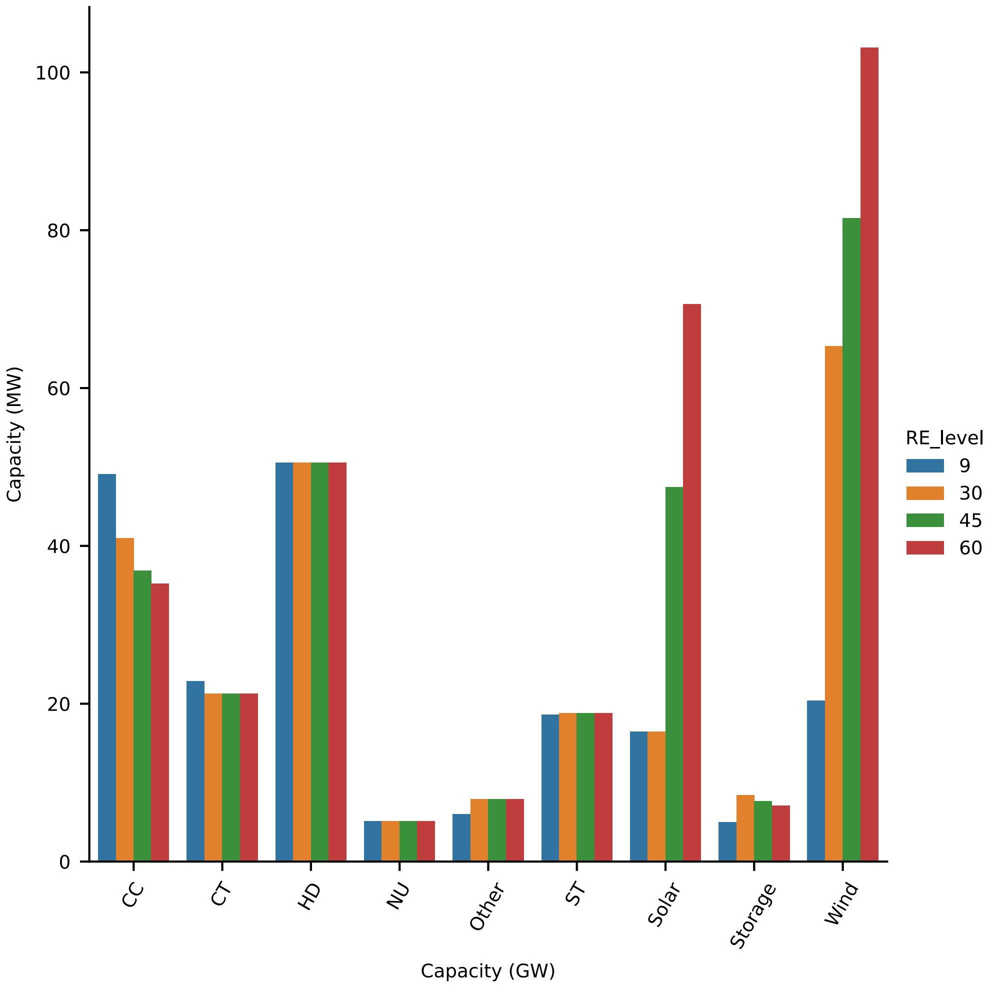

Fig. 2: **Installed capacities of different generation sources with increasing renewable penetrations for the 2019 weather year.** This figure shows WECC wide total capacities with color bars representing different RE penetrations.

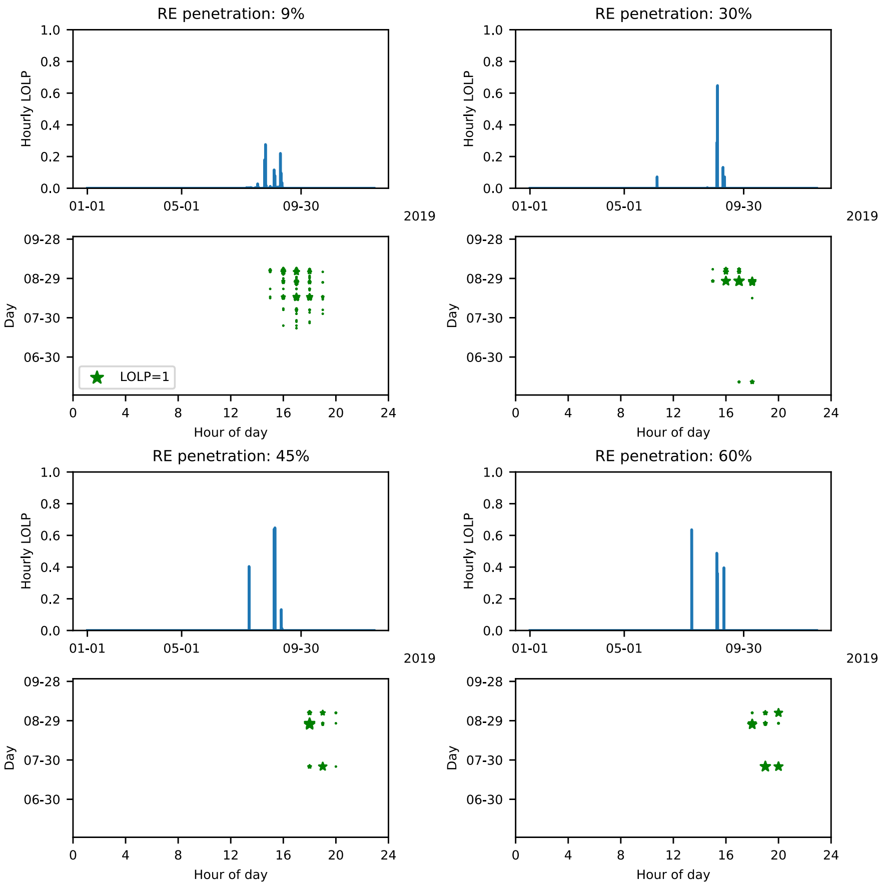

Fig. 3: **RA profiles and timing of RA failures.** For the 2019 weather year and for each renewable penetration, this figure shows, (i) hourly LOLPs across the entire year (i.e., the RA profile) and (ii) the date and hour of day (in PST) when RA failures occur, where the size of star is proportional to the LOLP and the legend shows marker size for LOLP=1. An LOLP of 0.1 indicates demand exceeds available capacity in 10% of the 250 simulated trials in the RA model.

To attribute RA failures to WPs, we map each risk hour to the prevailing weather regime, then quantify the number of risk hours and cumulative LOLP in each regime [Figure 4]. The cumulative LOLP equals the sum of LOLPs across hours mapped to a given weather regime, so is a function of the number of risk hours in a given weather regime and the LOLP in each of those hours. The cumulative LOLP also equals the expected loss of load hours (LOLH) attributed to each regime. Using either number of risk hours or cumulative LOLP metrics, WPs 6,7, and 8 predominantly drive RA failures across renewable penetrations [Figure 4]. These WPs correspond to high pressure anomalies that cover the entire Western US (as shown in Figure 1). Of those WPs, WP 8 accounts for most RA failures, e.g. 39-50% of risk hours and 54-82% of cumulative LOLP across renewable penetrations.

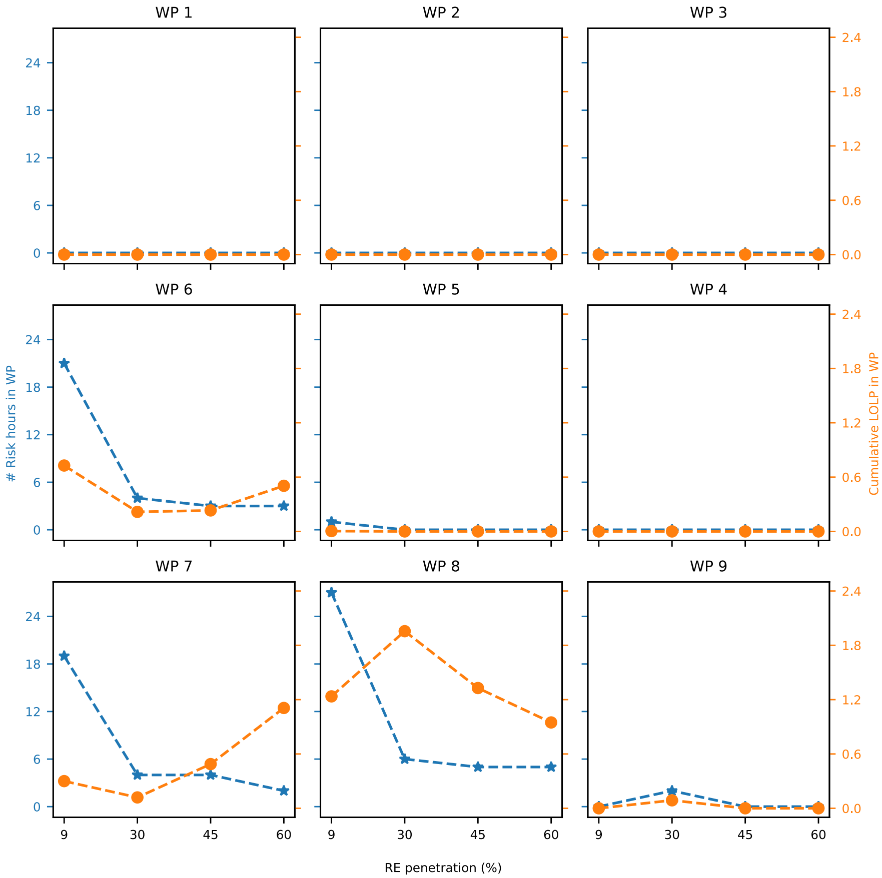

Fig. 4: **Risk hours and cumulative LOLP attributed to each weather regime in 2019.** For the 2019 weather year, for each renewable penetration this figure shows number of risk hours (blue lines) and cumulative LOLP (orange lines) attributed to each weather regime, where WPs correspond to figure 1.

The relative importance of WPs in driving RA failures is robust across increasing renewable penetrations for the 2019 weather year. As renewable penetrations increase from 9% to 60%, the number of risk hours driven by WP 8 decrease from 27 to 5, respectively, while the numbers of risk hours driven by WPs 6 and 7 exhibit an overall decrease, from 21 to 3 and from 19 to 2, respectively. Increasing renewable penetration has the opposite effect on cumulative LOLP driven by WPs 7 and 8. As renewable penetrations increase from 9% to 60%, the cumulative LOLP driven by WP 7 increases from 0.3 to 1.1, whereas cumulative LOLP driven by WP 8 decreases from 1.2 to 0.9 [Figure 4]. Cumulative LOLP driven by WP 6 shows an overall decrease from 0.7 to 0.5 comparing 9% and 60% renewable penetrations.

Mechanistically, surface meteorology, not high-pressure anomalies in the middle atmosphere, impact power system RA. To understand how the high pressure anomalies in WPs 6,7, and 8 drive RA failures, we analyze surface meteorology corresponding to each weather regime [ref. methods 4.4]. We find that these WPs correspond to positive surface temperature anomalies, and mixed surface solar radiation and wind speed anomalies across large regions of WECC [Figure 5]. Positive temperature anomalies lead to higher than average generator forced outages and demand. Concurrently, negative and low positive solar radiation anomalies lead to lower than average solar generation. While surface solar radiation anomalies are not negative across WECC in the 3 impactful weather patterns, in WP 7, these anomalies are negative in the CAMX region where a large fraction of solar capacity is installed [Figure 1]. WPs 6,7, and 8 also exhibit negative wind speed anomalies in large portions of the western US, and more notably so in WP 7. Each of these WPs include surface meteorology anomalies that reduce RA at low and high renewable penetrations, explaining the robustness of these three WPs in driving most RA failures at renewable penetrations ranging from 9% to 60%. Of these three WPs, WP 7 has increasingly drives total risk with increasing RE penetrations as it has the large positive temperature anomalies, largest negative solar anomaly over the Southwest, and largest negative wind speed anomaly over the entire region. Other WPs do not exhibit the same combination of surface temperature, wind speed, and solar radiation anomalies that WPs 6,7, and 8 do, explaining their relative unimportance in driving RA failures.

2.2 Meteorological drivers across different weather years

The above discussion examines drivers of RA failures across renewable penetrations for a single weather year, 2019. Given significant inter-annual variability in meteorology and climate, we repeat our above analysis across four weather years (2016 through 2019) or the duration of our combined data timeseries. This approach treats each meteorological year as an independent observation, allowing us to quantify the robustness of our results to different weather years.

Across weather years and RE penetrations, NGCC and wind capacities output by the CEM do not significantly differ across years. For instance, at 60% renewable penetration, NGCC capacities range from 45 to 35 GW, and wind capacities range from 95 to 116 GW across weather years [SI fig. A.9(a)]. Solar capacities exhibit a larger range across weather years, e.g., ranging from 27 GW in 2017 to 70 GW in 2019 at 60% RE penetration, with low solar capacity coinciding with high NGCC capacity [Figure SI.6(a)]. Storage capacity also exhibits a larger range, from 7 GW in 2019 to 19 GW in 2018. Our results

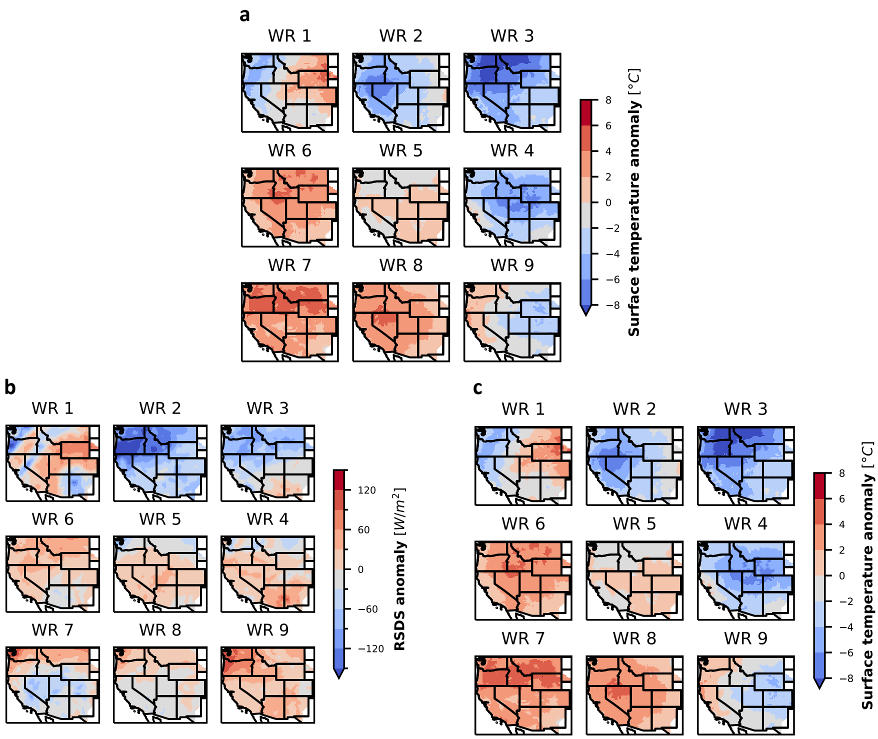

Fig. 5: **Surface meteorological anomalies corresponding to each weather regime** (a) Composites of surface temperature anomalies, (b) surface solar radiation anomalies, and (c) 100 m wind speeds anomalies for the 2019 weather year. The composites are constructed based on the hours from the 2019 extended summer belonging to each weather regime.

regarding the number of risk hours and maximum LOLPs are also largely insensitive to different weather years. Specifically, across weather years, risk hours decrease and maximum LOLPs increase between the current fleet and higher RE penetrations [SI fig. A.9(b)]. For instance, in 2018, risk hours decrease from 53 to 5 and maximum LOLPs increase from 0.3 to 0.96 when renewable penetrations increase from 9% to 60%. For all the weather years and renewable penetrations, we also simultaneously calculate the expected unserved energy (EUE). This is the sum of expected shortfall (in GWh) during each risk hour. SI fig. A.10 shows the EUE for the different systems with the effective shortfalls ranging from 3.5 GWh to 4.6 GWh and 1.1 GWH to 3 GWh at 9% and 60% RE penetrations respectively.

Meteorological drivers of RA failures are also robust to weather years [Figure 6]. WPs 6,7, and 8, which are high pressure anomalies, drive most RA failures across all weather years. Collectively, these WPs drive 87% to 100%

of all risk hours and 96% to 100% of cumulative LOLP across weather years. Furthermore, WP 7 emerges as an even more dominant driver of RA failures in 2016 through 2018 than in 2019. In weather years 2016 through 2018, WP 7 accounts for cumulative LOLPs of 84% to 100% of the respective scenario's total risk for renewable penetrations of 9% to 60%, compared to 13% to 43% in 2019 [Figure 6B]. When considering all days in the JJAS months, we find that the number of days attributed to the extreme weather patterns (WP 7 and WP 8, but particularly WP 7) are comparable to the number of days attributed to intermediate weather patterns (such as WPs 4, 5, and 6) [SI fig. A.6]. Moreover, among our study years, 2 years have above trend line occurrences of WPs 7 and 8, and 2 years have below trend line occurrences of WP 7. Despite the total number of days in each WP and variability in occurrence frequency among the years analyzed, WP7 emerges as the more dominant driver at higher RE penetrations across the weather years.

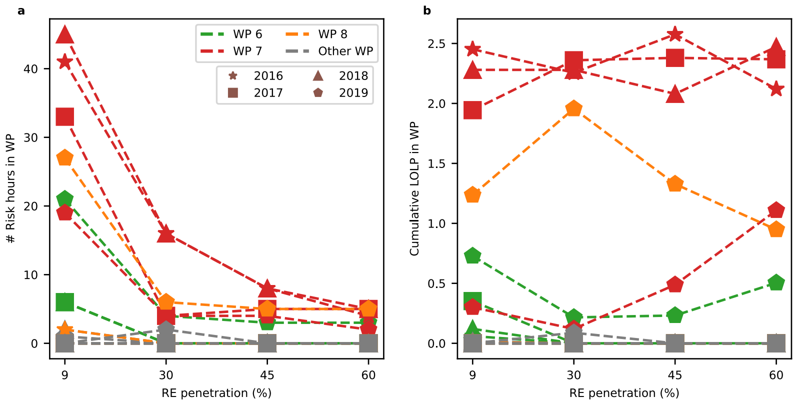

Fig. 6: **Risk hours and cumulative LOLP attributed to each weather regime across all weather years** a - Number of risk hours attributed to each weather regime across the weather years with increasing RE generation levels; b - Cumulative LOLP attributed to each weather regime across the weather years with increasing RE generation levels.

The surface meteorology associated with WPs 6,7, and 8 in weather years 2016-2018 show similar trends of positive temperature anomalies, negative wind speed anomalies, and mixed solar radiation anomalies in the Southwest as in 2019 [see SI figs. A11-13]. At higher RE penetrations, the risk is attributed to fewer days. So we look at the daily average temperature anomalies for these days [Figure 7]. Though these days are driven by WPs 6,7, or 8 across the weather years, they represent different distribution of surface meteorological anomalies in the different years. On the RA failure days, the temperature anomalies across these four years show predominantly positive anomalies over large portions of the region, but the magnitude, geographical location and extent of the positive anomalies vary. Some days also exhibit negative anomalies in some regions, but even on these days the anomalies are positive in the California region. SI figs. A.14 and A.15 show the surface solar radiation and wind speed anomalies for these days.

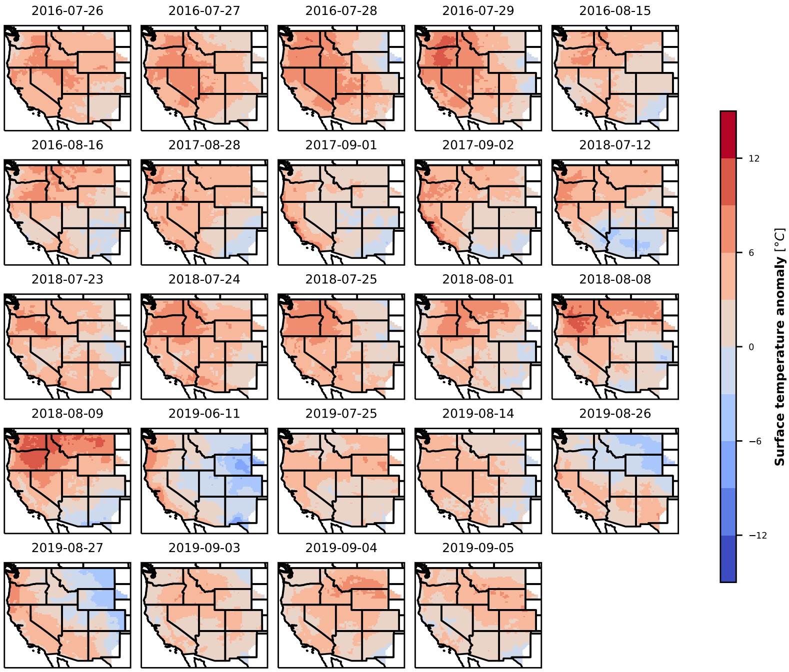

Fig. 7: **Daily surface temperature anomalies on days with RA failure events for RE penetrations from 30% to 60% across the weather years.** Each panel in this figure shows daily means of surface temperature anomalies on the RA failure days.

3 Discussion

Maintaining power system RA, and reliability more broadly, faces challenges from evolving supply- and demand-side technologies and non-stationary meteorology. In response to these challenges, this paper characterized meteorological drivers of RA failures by integrating power system and meteorological methods. We found that RA failures in WECC are driven by weather patterns corresponding to high pressure anomalies over the western United States.

The added value that our weather pattern approach gives over just a surface meteorological analysis is that we are able to capture the synoptic scale (1000-2500 km) drivers of the RA failure events. The weather patterns can be used in different ways to incorporate meteorological drivers of the power system in system planning as well as operations, as we move to interconnected continental scale systems. For system planning purposes, current practices mostly involve only using historical meteorological data with techniques like importance subsampling reducing computational costs by providing representative periods to the capacity expansion model [48]. Our findings can improve this subsampling process by providing a physical basis for choosing the representative periods. Further, to make informed investment decisions and maintain system reliability in the future, system planning needs to use future meteorological data from climate projections and the physics based subsampling procedure can help here as well. Future climate projections from global climate models have lower spatial and temporal resolution than required by power system models. Incorporating this future climate data requires computationally costly downscaling [16]. Our methods can reduce downscaling needs and associated costs by guiding selective downscaling of certain time periods of interest, e.g. time periods with high pressure anomalies in the Western US, to drive system planning and operation models. This can help system planners understand further risks, beyond resource adequacy, during these stressful periods. At the operational level, system operators, utilities, power producers, and communities can use the short term forecasts at the days to weeks timescale and long-range probabilistic forecasting at season-to-season time scale to avoid scheduling maintenance and other related down times when these patterns are expected to occur. These patterns are characterized by their temporal persistence and ability to represent meteorology at the synoptic scale during the occurrence of extreme events. These characteristics make the WPs more suitable, as an aggregate pointer to capture stressful periods for system operations, than individual surface meteorological variables, which exhibit higher spatio-temporal variations.

Rolling outages in California in the summer of 2020 support our results. On August 14 and 15, the California Independent System Operator (CAISO) instituted rotating electricity outages during an extreme heat storm covering much of the WECC system [4]. These rotating outages were necessitated by higher-than-predicted demand and supply shortages. While we are not able to include 2020 in our analysis due to data limitations, we can analyze atmospheric circulation prevailing during August 14 and 15 using our reanalysis data [Methods 4.5]. We find that the atmospheric circulation on these two days exhibits a high pressure anomaly over the Pacific northwest [SI fig. A.16] and resembles the high pressure WPs in our analysis. Our SOM identifies the circulation pattern on August 14 as belonging to WP 8 and on August 15 as belonging to WP 7. Thus, the CAISO rotating outage event provides real-world evidence for these weather patterns driving RA failures, which we have also identified through our analysis.

While outages threaten human health and well-being regardless of prevailing meteorology, outages during extreme heat can be particularly life threatening [17]. The robustness of high pressure anomalies driving RA failures at renewable penetrations up to 60% suggests that high temperature anomalies will continue to accompany RA failures. Consequences of outages could have disproportionate impacts on vulnerable populations [49], particularly when they align with extreme heat events [50]. Any disparities in outcomes during outages between income groups could widen as upper income individuals increasingly procure distributed energy systems. Our results indicate a long-term need to ensure vulnerable communities have access to potentially lifesaving cooling during outages, e.g., through investing in community hubs at public buildings [51].

Anthropogenic climate change is already affecting weather and climate, including by increasing surface air temperatures across the Western United States [52]. Using the ERA5 reanalysis dataset, we find some evidence for an increase in the frequency of weather regimes with high pressure anomalies from 1981 through 2020 in the extended summer months [SI fig. A.7]. During this period, WPs 7 and 8 (high pressure anomalies over northwest) occur more frequently, while some WPs like 3 and 4 (low pressure anomalies over northwest) occur less frequently. Increasing trend of WP 7 over the last 40 years are statistically significant (p-values less than 0.05) based on a simple linear regression with year as the independent variable and percent of days with the WP as the dependent variable. Specifically, WP7 shows an increase of 0.18 extended summer days per year. Given that we found high pressure anomalies, particularly WP7, drive RA failures, their increasingly frequent occurrence might result in more frequent challenges to maintaining RA. More rigorous analyses are needed to discern and attribute WP trends to aspects of the earth system dynamics, including natural variability versus anthropogenic changes. Emerging research has also found that the change in frequency of certain circulation pattern can compound climate extremes driven by anthropogenic warming [53]. So, better understanding how these impactful WPs will evolve and interact with a changing climate [26] would better inform the risk that climate change poses to RA.

Our research offers several opportunities for extensions. First, to capture covariability between supply and demand, our analysis is limited to four weather years. To capture long-term climate variability, future research could extend our analysis to multi-decadal timespans using historic data from reanalyses or future data from climate models. Second, future research could also incorporate decarbonization-driven changes on demand including electrification of residential heating and charging of electric vehicles. These extensions face several challenges, though, including estimating electricity demand with bottom-up models and obtaining high spatio-temporal resolution climate model outputs. Third, we do not consider the availability of flexible loads in our models, which can be an avenue for operational adjustments by the system operator to prevent RA failures. Incorporating these demand side changes could reduce the risk in hours with high failure susceptibility. Fourth, in linking specific weather patterns to resource adequacy failures, our research suggests climate downscaling methods designed, trained, and/or validated on these types of weather patterns could be highly valuable in bridging the disconnect between climate and energy system modelling [16]. Additionally, our results suggest RA analyses using future climate data could focus on weather regimes documented here, which could enable a greater computational focus on climate-related uncertainty.

4 Methods

4.1 Area of Study

Our area of study is the Western Interconnection, which is the region within the continental United States overseen by the Western Electricity Coordinating Council (WECC). We choose the WECC system for its high existing wind and solar installed capacities, its strong wind and solar resources, its large geographic area which makes it susceptible to large scale meteorology, and its vulnerability to climate change in the near-term. Climate change has already reduced system reliability in WECC, with extreme heat and drought exacerbated by climate change driving outages in California in 2020 [4]. We model WECC in terms of its constituent sub-regions in a representation similar to the one WECC uses in its western assessment of resource adequacy report. The five sub-regions are CAMX, Desert Southwest, Northwest Power Pool - Central (NWPP-Central), Northwest Power Pool - Northeast (NWPP-NE), Northwest Power Pool - Northwest (NWPP-NW). figure A.3 shows the geographic regions which are within the sub-regions [45].

4.2 Capacity Expansion

We use a capacity expansion model (CEM) to create future WECC generator fleets that meet increasing renewable generation requirements. We run the CEM for each analyzed weather year, capturing coincident, spatially-resolved meteorology and hydrology for each year. The CEM is a deterministic linear program that minimizes fixed plus variable costs by deciding investment in wind, solar, 4-hour utility-scale battery storage, and inter-regional transmission, and operation of existing and new generators, storage, and inter-regional transmission. Wind and solar capacity investment decisions occur at the spatial resolution of our wind and solar resource data, i.e. on a 30 by 30 km grid across WECC, while storage and transmission investments occur at the five-region and inter-regional levels, respectively. Because we couple the CEM with the RAM (described below), which adds or removes thermal generators from each future fleet to meet a given reliability target, we do not add thermal units or retire any existing units in the CEM. Thus, the fleets generated from the CEM form a basis for creating the final fleets used in our analysis. These final fleets are obtained after the RAM adds or removes thermal generators.

The CEM includes numerous system- and generator-level constraints. At the system level, the CEM requires total generation to meet demand in each hour. To approximate system reliability standards, the CEM includes a 13%

planning reserve margin, which requires derated capacity to exceed peak demand by at least 13%. Derated capacity accounts for hourly wind and solar generation potential during the peak demand hour, a fixed 5% forced outage rate for wind and solar generators, and for temperature-dependent forced outage rates for all other generator types (see SI section 3.3 for forced outage rates used) [10]. At the generator level, generation can vary between zero and maximum capacities, following engineering and economic-based unit operations constraints. Wind and solar generation is also limited by hourly, spatially-specific wind and solar capacity factors (see 4.5). The CEM also decides and constrains hourly charging, discharging, and state of charge of each existing and new storage unit. To examine generator fleets with increasing RE penetrations, the CEM requires total WECC-wide wind plus solar generation to meet a percent of total annual demand (see section 4.6 for specification of target levels).

For computational tractability, we run the CEM in hourly intervals for one representative time block per season, with seven sequential days in each time block, and for days with peak annual demand, net demand, and upwards hourly ramp. The representative days capture typical operations and costs, while the peak days capture system capacity and flexibility investment needs. Sampled representative days per season minimize the root mean squared error between sampled and seasonal net demand profiles. Within each time block, the CEM dispatches regional hydropower generation based on historic year-specific generation data.

We formulate the CEM using the General Algebraic Modeling System [54] and solve it using CPLEX [55]. For the full CEM formulation and description, see SI section 2.

4.3 Resource Adequacy Model

To quantify resource adequacy on an hourly and annual basis, we combine a Monte-Carlo-based non-sequential state sampling procedure with an optimization-based sequential storage dispatch procedure. The state sampling procedure randomly samples forced outages at each generator within every WECC sub-region in each hour of the year 250 times via Monte Carlo simulation (see SI section 3.2 for justification of sample size). This results in 250 independent capacity curves for the year, each of which are paired with observed hourly demand for the year. Like in the CEM, forced outages are a function of location-specific ambient air temperatures for thermal and hydropower plants [10], are a constant rate of (0.05) for solar and wind plants [46], and are assumed to be zero for storage and transmission (see SI section 3.3 for forced outage rates used).

Within each sub-region, for each capacity curve after storage dispatch occurs, we identify hours where any sub-region has a loss of load event (where sub-regional demand exceeds available sub-regional generation). For these hours we run a simple network flow optimization problem to determine inter-regional transfers within each Monte Carlo iteration. The optimization objective is to minimize the total cost of energy transfer along the lines and cost of energy not served within the sub-regions, with constraints imposed on line limits and energy available for export from each sub-region (see SI section 3.1 for transmission optimization formulation). Following this procedure, we obtain an RA profile for each sub-region, which is the hourly loss of load probability (LOLP) time series. This RA profile contains the fraction of Monte Carlo iterations which resulted in a loss of load event in each hour. We refer to any hour with a $LOLP > 0$ to be a risk hour. As we find the LOLP time series, we also simultaneously calculate the expected hourly shortfall time series and the total expected unserved energy (EUE). The expected hourly shortfall is the sum of (load - generation) for those trials when load exceeds generation, divided by the total number of trials. EUE is the sum of this hourly expected shortfall.

Unlike our RAM, our CEM does not account for stochastic outages. Instead, the CEM aims to produce a resource adequate system by enforcing a planning reserve margin. To facilitate resource adequacy comparisons across future systems output by our CEM, our RAM adjusts the generation fleets in CAMX for each case we model so that each fleet's annual resource adequacy achieves a target value. Specifically, the RAM iteratively adds or removes NGCC capacity in CAMX then calculates annual resource adequacy until the annual loss of load hours ($LOLH = \sum(LOLP)$) is 2.4 in each case. This target value reflects the real-world 1-in-10 reliability standard widely adopted by utilities. Due to high computational time taken to obtain the RA profiles and apriori unknown number of addition/removal trials of NGCC capacity, the iterative procedure is performed with 50 Monte Carlo samples at each stage. This means that the final fleets all do not have an exact LOLH = 2.4, but vary between LOLH = 2 to LOLH = 2.6. After each generator fleet is adjusted, the RAM estimates the fleet's hourly and annual resource adequacy. We use CAMX as the subregion of interest as it shows highest LOLH across the scenarios modeled and the timing of RA failure in other regions coincide with RA failures in CAMX.

Inputs to the RAM include the generator fleets output by the CEM; hourly surface air temperatures; and forced outage rates. The CEM provides location and sub-region specific installed capacities for all generators and storage. The CEM has various generators, but in going from CEM to RAM we retain these generators as such, but combine - pumped hydro, batteries, fuel cell to *storage* type; and geothermal, different types of waste, biomass, and other small fossil generators *other* type.

Prior to the stochastic simulation procedure, we calculate the hydroelectric generation for each scenario within each sub-region. For each of our five regions in WECC, we obtain monthly hydropower generation from EIA-923 data, then calculate subregional contribution proportional to installed capacity. To estimate hourly generation, we then carry out a greedy dispatch procedure for each month. The algorithm first quantifies hourly electricity demand not met by every generator other than hydropower and storage units (i.e., residual demand). The algorithm then dispatches hydropower units on a consecutive hourly basis. In each hour, the algorithm sets regional hydropower generation equal to the minimum of residual demand and regional total installed hydropower capacity, provided cumulative monthly generation through each hour doesn't exceed monthly generation limits. Any leftover monthly generation in the month is redistributed to all hours proportional to electricity demand minus wind and solar generation (i.e., net demand).

4.4 Meteorological Analysis

Weather Regimes

To characterize meteorological drivers of risk hours, we begin by identifying the weather regimes and corresponding circulation patterns that coincide with risk hours. To identify weather regimes in our study region (WECC), we use self-organizing maps (SOMs), which is an unsupervised neural-network-based clustering technique. Unlike other hierarchical and non-hierarchical clustering techniques, SOMs cluster input data into nodes that form a topological representation in which node proximity indicates their similarity. Previous studies have identified weather regimes with SOMs in other contexts, e.g. to quantify the frequency and persistence of weather regimes associated with heat waves [56] and extreme precipitation events [57] in a warming climate.

We create our SOMs using seasonal anomalies of the daily average 500 hPa geopotential height (Z500) for the extended summer season (June through September, or JJAS) from 1981-2020. We analyze an extended summer season because our risk hours occur in June through September, so we focus on the warmest months of the year without narrowly constraining our SOMs to a small subset of months. We use Z500 because it captures synoptic-scale atmospheric processes and their relationship with surface meteorology, is persistent over multiple days, and is widely used for weather typing in the US and Europe [25, 32, 58, 59]. To produce the SOM, we use the MiniSom Python package [60] with the following parameterization: grid shape of 3 rows and 3 columns, a *gaussian* neighborhood function, sigma (i.e., spread of neighborhood function) value of 1, learning rate of 0.1, and 5,000 training iterations. These parameter values provide a concise weather regime representation that balances quantization and topographic error [see SI section 4]. SI fig. A.6 shows the total number of days attributed to each weather pattern over the 40 year period used to train the SOM. Since the objective of weather patterning is not to get an equal number of elements in each node, but to cluster weather patterns based on similarity, the number of days assigned to all weather patterns are not equal.

Surface Meteorology

While daily Z500 anomalies are a meaningful variable for weather regime identification via SOMs, the power system is directly affected not by Z500 but rather by surface meteorological variables. Thus, we study surface meteorology corresponding to the weather regimes as well as surface meteorology on the RA failure days for the different years. For each weather regime identified by our SOM, we make composite maps of hourly anomalies in surface temperature, surface solar radiation, and near surface wind speed. To calculate these hourly anomalies, we calculate the JJAS seasonal hour-of-day mean of surface weather data for each year (yielding 24 mean values for each year), then subtract this seasonal hour-of-day mean from each hourly data point within the years. We analyse anomalies within the year rather over the 40-year period as our models work with a yearly time series and that the investment decisions are made to cater to that year. Using the hourly anomalies, we construct composite maps for the weather years (2016-2019) in a two step process. First, we map each day from the extended summer months to a weather regime by passing daily Z500 anomaly into the SOM. Second, for every hour of each day that belong to each weather regime, we average the hourly surface meteorology anomalies to get the composite surface meteorological anomalies under each weather regime. For solar radiation anomaly composites, we choose only the daylight hours region wide (6AM to 8PM PST) to avoid biasing the composites towards the hours with very low solar radiation. To capture surface meteorology directly driving the RA failure days, we find the unique days when these events occur across the four weather years analysed at RE penetrations of 30% or more, and plot the mean surface meteorology anomaly in those days. Here too, for solar radiation anomalies we use only the daylight hours.

4.5 Data Description

Demand Data

We get hourly sub-regional electricity demand from a database of screened and imputed data based on observed demand [44]. Due to limited availability of observed hourly electricity demand, the database provides four full years of balancing authority (BA) level demand from 2016 through 2019, and subregional demand is constructed by aggregating demand from BAs within each subregion [ref. SI section 2.6.1]. Though there are techniques to backcast electricity demand based on meteorological and societal factors, these methods exhibit large errors, particularly in predicting extreme demand values [7, 61]. Since demand extremes are a major factor in RA, we opt for observational rather than backcasted demand values.

ERA5 Reanalysis Data

Given that identification of weather regimes requires long-term (multi-decadal) weather data, we use reanalysis weather data for our analysis. Specifically, we obtain weather data from the ERA5 reanalysis dataset [62]. The weather data used for surface meteorological anomalies and weather pattern identification for each weather year coincides with the weather data used to drive the power system models for the corresponding weather year. We choose ERA5 because it provides wind speeds at 100 m above surface at hourly resolution, unlike other reanalyses products [63]. ERA5 is also widely used in power systems and synoptic meteorology research [24, 34, 35]. From ERA5, we specifically obtain near-surface air temperature (t2m); dewpoint temperature (tdps); air pressure (sp); zonal and meridional surface wind speeds (u10 & v10); downward shortwave solar radiation at the surface (ssrd); and zonal and meridional wind speeds at 100m level (u100 & v100). We obtain each data field at hourly temporal resolution and 30 km spatial resolution.

Capacity Factors

We derive solar capacity factors directly from the surface downwelling shortwave radiation data for a EFG-Polycrystalline silicon photovoltaic module using the formulation described by Jerez et. al. [64] [See SI section 1.1]. We calculate wind capacity factors using the formulation described by Karnauskas et. al. [65] and the composite 1.5 MW IEC class III turbine from the System Advisor Model [66] [See SI section 1.2].

Technology and Costs

We obtain operational costs for existing generators from the NREL Annual Technology Baseline (ATB) moderate technology development scenario for 2030 [67], and fuel costs from the EIA annual energy outlook for 2020 [68]. For new units which the CEM determines investment in, we obtain capital costs from the ATB.

4.6 Scenarios

To capture the effect of increasing renewable penetrations on meteorological drivers of reliability, we run four scenarios of increasing wind plus solar penetrations: 9% (based on the current fleet), 30%, 45%, and 60%. These scenarios are enforced in the CEM by constraining constraining annual wind plus solar generation to equal to a percentage of annual electricity demand. Given significant inter-annual variability in meteorology and climate, we run our modeling framework for each renewable scenario for each year of available electricity demand data (2016 through 2019). This approach treats each meteorological year as an independent observation, allowing us to quantify the robustness of our results to different weather years.

While our results are based on fleets built for specified renewable penetrations, we have also explored publicly available datasets for understanding the plausibility of the fleets we have obtained. One of these, the WECC anchor dataset (ADS), provides generator fleet and hourly load and renewable generation shapes for 2032. The ADS renewable penetration percent is 32% with total installed capacity of 60GW in utility scale solar PV and 38GW of on-shore wind generation, which falls within our renewable penetration and installed generation ranges studied. While our methods can also be applied to that dataset to understand the meteorological drivers, we have not done so in this paper for conciseness.

Author Contributions

SS-Conceptualized and designed research, analyzed data, developed analytical pipeline, wrote paper; MC-Conceptualized, designed and supervised research, wrote paper, provided funding; AP-Conceptualized, designed, and supervised research, revised paper; FL, DB-Supervised research, revised paper

Competing Interests

The authors have no competing interests to declare.

Data availability

Meteorological, power system output from the models, and code used to create the final figures in the manuscript are available via Zenodo [69].

Code availability

Code for the CEM and RAM used in this study is available online via Zenodo [70].

Acknowledgments. This work was supported by the National Science Foundation under the Award #2142421. SS thanks Dr. An Pham for her help with the CEM formulation & code and Isaac Bromley-Dulfano for help with the RAM. The results contain modified Copernicus Climate Change Service information 2020. Neither the European Commission nor ECMWF is responsible for any use that may be made of the Copernicus information or data it contains.

Correspondence. To whom correspondence should be addressed. E-mail: sriharis@umich.edu, mtcraig@umich.edu

References

[1] Desa, U.N.: Transforming our world: The 2030 agenda for sustainable development (2016)

[2] Pérez-Arriaga, I.J.: Regulation of the Power Sector. Springer, ??? (2014)

[3] North American Electric Reliability Corporation: 2021 Long-Term Reliability Assessment (2021). https://www.nerc.com/pa/RAPA/ra/Pages/default.aspx

[4] CPUC, CAISO, CEC: Root Cause Analysis: Mid-August 2020 Extreme Heat Wave (2021). http://www.caiso.com/Documents/Final-Root-Cause-Analysis-Mid-August-2020-Extreme-Heat-Wave.pdf

[5] Mays, J., Craig, M.T., Kiesling, L., Macey, J.C., Shaffer, B., Shu, H.: Private risk and social resilience in liberalized electricity markets. Joule (2022)

[6] Auffhammer, M., Baylis, P., Hausman, C.H.: Climate change is projected to have severe impacts on the frequency and intensity of peak electricity demand across the united states. Proceedings of the National Academy of Sciences **114**(8), 1886–1891 (2017)

[7] Ralston Fonseca, F., Jaramillo, P., Bergés, M., Severnini, E.: Seasonal effects of climate change on intra-day electricity demand patterns. Climatic Change **154**(3), 435–451 (2019)

[8] Zhai, H., Rubin, E.S., Versteeg, P.L.: Water use at pulverized coal power plants with postcombustion carbon capture and storage. Environmental science & technology **45**(6), 2479–2485 (2011)

[9] Loew, A., Jaramillo, P., Zhai, H., Ali, R., Nijssen, B., Cheng, Y., Klima, K.: Fossil fuel–fired power plant operations under a changing climate. Climatic Change **163**(1), 619–632 (2020)

[10] Murphy, S., Sowell, F., Apt, J.: A time-dependent model of generator failures and recoveries captures correlated events and quantifies temperature dependence. Applied Energy **253**, 113513 (2019)

[11] Kumler, A., Carreño, I.L., Craig, M.T., Hodge, B.M., Cole, W., Brancucci, C.: Inter-annual variability of wind and solar electricity generation and capacity values in Texas. Environ. Res. Lett. **14**(4) (2019). https://doi.org/10.1088/1748-9326/aaf935

[12] Haupt, S.E., Copeland, J., Cheng, W.Y.Y., Zhang, Y., Ammann, C., Sullivan, P.: A method to assess the wind and solar resource and to quantify interannual variability over the United States under current and projected future climate. J. Appl. Meteorol. Climatol. **55**(2), 345–363 (2016). https://doi.org/10.1175/JAMC-D-15-0011.1

[13] Jia, B., Xie, Z., Dai, A., Shi, C., Chen, F.: Evaluation of satellite and reanalysis products of downward surface solar radiation over east asia: Spatial and seasonal variations. Journal of Geophysical Research: Atmospheres **118**(9), 3431–3446 (2013)

[14] Zhang, J., Hodge, B.-M., Gomez-Lazaro, E., Lovholm, A.L., Berge, E., Miettinen, J., Holttinen, H., Cutululis, N., Litong-Palima, M., Sorensen, P., et al.: Analysis of variability and uncertainty in wind power forecasting: an international comparison. Technical report, National Renewable Energy Lab.(NREL), Golden, CO (United States) (2013)

[15] Kotamarthi, R., Hayhoe, K., Mearns, L.O., Wuebbles, D., Jacobs, J., Jurado, J.: Downscaling Techniques for High-Resolution Climate Projections: From Global Change to Local Impacts. Cambridge University Press, ??? (2021). https://doi.org/10.1017/9781108601269

[16] Craig, M.T., Wohland, J., Stoop, L.P., Kies, A., Pickering, B., Bloomfield, H.C., Browell, J., De Felice, M., Dent, C.J., Deroubaix, A., et al.: Overcoming the disconnect between energy system and climate modeling. Joule (2022)

[17] Stone Jr, B., Mallen, E., Rajput, M., Gronlund, C.J., Broadbent, A.M., Krayenhoff, E.S., Augenbroe, G., O'Neill, M.S., Georgescu, M.: Compound climate and infrastructure events: how electrical grid failure alters heat wave risk. Environmental Science & Technology **55**(10), 6957–6964 (2021)

[18] Goodess, C.M., Palutikof, J.P.: Development of daily rainfall scenarios for southeast spain using a circulation-type approach to downscaling. International Journal of Climatology: A Journal of the Royal Meteorological Society **18**(10), 1051–1083 (1998)

[19] Soares, P.M., Maraun, D., Brands, S., Jury, M., Gutiérrez, J.M., San-Martín, D., Hertig, E., Huth, R., Belušić Vozila, A., Cardoso, R.M., *et al.*: Process-based evaluation of the value perfect predictor experiment of statistical downscaling methods. International Journal of Climatology **39**(9), 3868–3893 (2019)

[20] White, C.J., Domeisen, D.I., Acharya, N., Adefisan, E.A., Anderson, M.L., Aura, S., Balogun, A.A., Bertram, D., Bluhm, S., Brayshaw, D.J., et al.: Advances in the application and utility of subseasonal-to-seasonal predictions. Bulletin of the American Meteorological Society, 1–57 (2021)

[21] Michelangeli, P.-A., Vautard, R., Legras, B.: Weather regimes: Recurrence and quasi stationarity. Journal of the atmospheric sciences **52**(8), 1237–1256 (1995)

[22] Casola, J.H., Wallace, J.M.: Identifying weather regimes in the wintertime 500-hpa geopotential height field for the pacific–north american sector using a limited-contour clustering technique. Journal of applied meteorology and climatology **46**(10), 1619–1630 (2007)

[23] Adams, R.E., Lee, C.C., Smith, E.T., Sheridan, S.C.: The relationship between atmospheric circulation patterns and extreme temperature events in north america. International Journal of Climatology **41**(1), 92–103 (2021)

[24] Rogers, C.D., Kornhuber, K., Perkins-Kirkpatrick, S.E., Loikith, P.C.,

Singh, D.: Sixfold increase in historical northern hemisphere concurrent large heatwaves driven by warming and changing atmospheric circulations. Journal of Climate **35**(3), 1063–1078 (2022)

[25] Agel, L., Barlow, M., Skinner, C., Colby, F., Cohen, J.: Four distinct northeast us heat wave circulation patterns and associated mechanisms, trends, and electric usage. npj Climate and Atmospheric Science **4**(1), 1–11 (2021)

[26] Fabiano, F., Meccia, V.L., Davini, P., Ghinassi, P., Corti, S.: A regime view of future atmospheric circulation changes in northern mid-latitudes. Weather and Climate Dynamics **2**(1), 163–180 (2021)

[27] Faranda, D., Vrac, M., Yiou, P., Jézéquel, A., Thao, S.: Changes in Future Synoptic Circulation Patterns: Consequences for Extreme Event Attribution. Geophysical Research Letters **47**(15), 1–9 (2020). https://doi.org/10.1029/2020GL088002

[28] Palipane, E., Grotjahn, R.: Future projections of the large-scale meteorology associated with california heat waves in cmip5 models. Journal of Geophysical Research: Atmospheres **123**(16), 8500–8517 (2018)

[29] Francis, J.A., Skific, N., Vavrus, S.J.: North American Weather Regimes Are Becoming More Persistent: Is Arctic Amplification a Factor? Geophysical Research Letters **45**(20), 11414–11422 (2018). https://doi.org/10.1029/2018GL080252

[30] Bloomfield, H., Suitters, C., Drew, D.: Meteorological drivers of european power system stress. Journal of Renewable Energy **2020** (2020)

[31] Brown, P.T., Farnham, D.J., Caldeira, K.: Meteorology and climatology of historical weekly wind and solar power resource droughts over western north america in era5. SN Applied Sciences **3**(10), 1–12 (2021)

[32] van der Wiel, K., Stoop, L.P., Van Zuijlen, B., Blackport, R., Van den Broek, M., Selten, F.: Meteorological conditions leading to extreme low variable renewable energy production and extreme high energy shortfall. Renewable and Sustainable Energy Reviews **111**, 261–275 (2019)

[33] Brayshaw, D.J., Dent, C., Zachary, S.: Wind generation's contribution to supporting peak electricity demand–meteorological insights. Proceedings of the Institution of Mechanical Engineers, Part O: Journal of Risk and Reliability **226**(1), 44–50 (2012)

[34] van der Wiel, K., Bloomfield, H.C., Lee, R.W., Stoop, L.P., Blackport, R., Screen, J.A., Selten, F.M.: The influence of weather regimes on european renewable energy production and demand. Environmental Research

Letters **14**(9), 094010 (2019)

[35] Bloomfield, H.C., Brayshaw, D.J., Charlton-Perez, A.J.: Characterizing the winter meteorological drivers of the european electricity system using targeted circulation types. Meteorological Applications **27**(1), 1858 (2020)

[36] Pickering, B., Grams, C.M., Pfenninger, S.: Sub-national variability of wind power generation in complex terrain and its correlation with large-scale meteorology. Environmental Research Letters **15**(4) (2020). https://doi.org/10.1088/1748-9326/ab70bd

[37] Lueken, R., Apt, J., Sowell, F.: Robust resource adequacy planning in the face of coal retirements. Energy Policy **88**, 371–388 (2016)

[38] Ibanez, E., Milligan, M.: Comparing resource adequacy metrics and their influence on capacity value. In: 2014 International Conference on Probabilistic Methods Applied to Power Systems (PMAPS), pp. 1–6 (2014). IEEE

[39] Bromley-Dulfano, I., Florez, J., Craig, M.T.: Reliability benefits of wide-area renewable energy planning across the western united states. Renewable Energy **179**, 1487–1499 (2021)

[40] Pickering, S., Rostkowski, I., Foley, S., Huebsch, M., Claes, Z., Ticknor, D., McCalley, J., Okullo, J., Heath, B., Figueroa-Acevedo, A.: Power system resource adequacy evaluation under increasing renewables for the midwestern us. In: 2019 North American Power Symposium (NAPS), pp. 1–6 (2019). IEEE

[41] Ibanez, E., Milligan, M.: Impact of transmission on resource adequacy in systems with wind and solar power. In: 2012 IEEE Power and Energy Society General Meeting, pp. 1–5 (2012). IEEE

[42] Turner, S.W.D., Voisin, N., Fazio, J., Hua, D., Jourabchi, M.: Compound climate events transform electrical power shortfall risk in the Pacific Northwest. Nat. Commun. **10**(1) (2019). https://doi.org/10.1038/s41467-018-07894-4

[43] WECC: August 2020 Heatwave Event Analysis Report (2021). https://www.wecc.org/Reliability/August%202020%20Heatwave%20Event%20Report.pdf

[44] Ruggles, T.H., Farnham, D.J., Tong, D., Caldeira, K.: Developing reliable hourly electricity demand data through screening and imputation. Scientific data **7**(1), 1–14 (2020)

[45] WECC: Western Assessment of Resource Adequacy (2022). https://www.wecc.org/Reliability/2022%20Western%20Assessment%20of%20Resource%20Adequacy.pdf

[46] Kashefi Kaviani, A., Riahy, G.H., Kouhsari, S.M.: Optimal design of a reliable hydrogen-based stand-alone wind/pv generating system, considering component outages. Renewable Energy **34**(11), 2380–2390 (2009). https://doi.org/10.1016/j.renene.2009.03.020

[47] Evans, M.P., Tindemans, S.H., Angeli, D.: Minimizing unserved energy using heterogeneous storage units. IEEE Transactions on Power Systems **34**(5), 3647–3656 (2019)

[48] Hilbers, A.P., Brayshaw, D.J., Gandy, A.: Importance subsampling: improving power system planning under climate-based uncertainty. Applied Energy **251**, 113114 (2019)

[49] Busby, J.W., Baker, K., Bazilian, M.D., Gilbert, A.Q., Grubert, E., Rai, V., Rhodes, J.D., Shidore, S., Smith, C.A., Webber, M.E.: Cascading risks: Understanding the 2021 winter blackout in texas. Energy Research & Social Science **77**, 102106 (2021)

[50] Klinenberg, E.: Heat Wave: A Social Autopsy of Disaster in Chicago. University of Chicago press, ??? (2015)

[51] Farthing, A., Craig, M., Reames, T.: Optimizing solar-plus-storage deployment on public buildings for climate, health, resilience, and energy bill benefits. Environmental Science & Technology **55**(18), 12528–12538 (2021)

[52] Vose, R., Easterling, D.R., Kunkel, K., LeGrande, A., Wehner, M.: Temperature changes in the united states. Climate science special report: fourth national climate assessment **1**(GSFC-E-DAA-TN49028) (2017)

[53] Faranda, D., Messori, G., Jezequel, A., Vrac, M., Yiou, P.: Atmospheric circulation compounds anthropogenic warming and impacts of climate extremes in europe. Proceedings of the National Academy of Sciences **120**(13), 2214525120 (2023)

[54] GAMS Development Corporation: General Algebraic Modeling System (GAMS) Release 36.1.0 (2021). https://www.gams.com/latest/docs/RN_36.html

[55] International Business Machines Corporation: IBM CPLEX 20.1.2021 (2021). https://www.ibm.com/docs/en/icos/20.1.0

[56] Horton, D.E., Johnson, N.C., Singh, D., Swain, D.L., Rajaratnam, B.,

Diffenbaugh, N.S.: Contribution of changes in atmospheric circulation patterns to extreme temperature trends. Nature **522**(7557), 465–469 (2015)

[57] Loikith, P.C., Lintner, B.R., Sweeney, A.: Characterizing large-scale meteorological patterns and associated temperature and precipitation extremes over the northwestern United States using self-organizing maps. Journal of Climate **30**(8), 2829–2847 (2017). https://doi.org/10.1175/JCLI-D-16-0670.1

[58] Loikith, P.C., Broccoli, A.J.: Characteristics of observed atmospheric circulation patterns associated with temperature extremes over north america. Journal of Climate **25**(20), 7266–7281 (2012)

[59] Cassou, C.: Intraseasonal interaction between the madden–julian oscillation and the north atlantic oscillation. Nature **455**(7212), 523–527 (2008)

[60] Vettigli, G.: MiniSom: minimalistic and NumPy-based implementation of the Self Organizing Map (2018). https://github.com/JustGlowing/minisom/

[61] Ghosh, R.: Data-driven stochastic reliability assessment of the us electricity grid under large penetration of variable renewable energy resources. PhD thesis, Carnegie Mellon University (January 2022). https://doi.org/10.1184/R1/17939732.v1. https://kilthub.cmu.edu/articles/thesis/Data-driven_stochastic_reliability_assessment_of_the_US_electricity_grid_under_large_penetration_of_variable_renewable_energy_resources/17939732

[62] Hersbach, H., Bell, B., Berrisford, P., Biavati, G., Horányi, A., Muñoz Sabater, J., Nicolas, J., Peubey, C., Radu, R., Rozum, I., et al.: Era5 hourly data on single levels from 1979 to present. Copernicus Climate Change Service (C3S) Climate Data Store (CDS) **10** (2018)

[63] Olauson, J.: Era5: The new champion of wind power modelling? Renewable energy **126**, 322–331 (2018)

[64] Jerez, S., Tobin, I., Vautard, R., Montávez, J.P., López-Romero, J.M., Thais, F., Bartok, B., Christensen, O.B., Colette, A., Déqué, M., *et al.*: The impact of climate change on photovoltaic power generation in europe. Nature communications **6**(1), 1–8 (2015)

[65] Karnauskas, K.B., Lundquist, J.K., Zhang, L.: Southward shift of the global wind energy resource under high carbon dioxide emissions. Nature Geoscience **11**(1), 38–43 (2018)

[66] Blair, N., Diorio, N., Freeman, J., Gilman, P., Janzou, S., Neises, T., Wagner, M.: System advisor model (sam) general description (version 2017.9.5). National Renewable Energy Laboratory Technical Report (2018)

[67] Akar, S., Beiter, P., Cole, W., Feldman, D., Kurup, P., Lantz, E., Margolis, R., Oladosu, D., Stehly, T., Rhodes, G., et al.: 2020 annual technology baseline (atb) cost and performance data for electricity generation technologies. Technical report, National Renewable Energy Laboratory-Data (NREL-DATA), Golden, CO (United ... (2020)

[68] AEO: Annual Energy Outlook 2020. Online (2020). https://www.eia.gov/outlooks/aeo/pdf/AEO2020%20Full%20Report.pdf

[69] Sundar, S., Craig, M., Payne, A., Brayshaw, D., Lehner, F.: MD-RA-USWEST_data. https://doi.org/10.5281/zenodo.8076307. https://doi.org/10.5281/zenodo.8076307

[70] Sundar, S.: sriharisundar/MD-RA-USWEST. https://doi.org/10.5281/zenodo.8076321. https://doi.org/10.5281/zenodo.8076321

Supplementary Information for Meteorological Drivers of Resource Adequacy Failures in Current and High Renewable Western U.S. Power Systems

August 2, 2023

1 Capacity factors

1.1 Solar

We derive hourly solar capacity factors for a EFG-Polycrystalline silicon photovoltaic module as[1]:

$$CF^t_{pv} = P^t_R \frac{RSDS^t}{RSDS_{STC}} \tag{A.1}$$

where $RSDS^t$ hourly represents surface downwelling shortwave flux in air $[Wm^{-2}]$ for which we use the *surface solar radiation downwards* variable from ERA5, and the superscript t indexes the hour. Though the variable is referred with short name *SSRD* in ERA5 datasets, we refer to it as *RSDS* following the CF conventions used in climate model intercomparison projects (CMIP) and in various literature. In ERA5 data, this quantity is captured as hourly energy accumulation with units Jm^{-2} but we need to calculate power derived from solar radiation, so we divide hourly accumulation by $3600s$ to obtain the average power during the hour with units Wm^{-2} [1]. All the metorological variables are discreet in time and space (at the dataset resolution), and the index t is dropped hereafter for conciseness. In eq.A.1, $RSDS_{STC}$ refers to RSDS at standard test conditions and is equal to $1000Wm^{-2}$, and P^t_R is the hourly performance ratio calculated using

$$P_R = 1 + \gamma[T_{cell} - T_{STC}] \tag{A.2}$$

$$T_{cell} = c_1 + c_2 TAS + c_3 RSDS + c_4 SWS \tag{A.3}$$

where T_{cell} is the PV cell temperature, TAS is surface air temperature (*2m temperature* in ERA5, converted from K to °C), and SWS is surface wind speed (calculated from *10m u- and v- components of wind* from ERA5). In eq.A.2, $\gamma = -0.005°C^{-1}$ and $T_{STC} = 25°C$. In eq.A.3, $c_1 = 4.3°C,\ c_2 = 0.943,\ c_3 = 0.028°Cm^2W^{-1}$, and $c_4 = -1.528°Csm^{-1}$ [2].

1.2 Wind

We calculate wind capacity factors using the formulation described in [3] for the composite 1.5 MW IEC class III turbine with power curves from the System Advisor Model (SAM) [4] as:

$$CF^t_{wind} = p(W^t_{100}) \tag{A.4}$$

where p is a function describing the power curve and W^t_{100} is the hourly corrected 100m wind speed. The correction accounts for air density and humidity related effects on the wind turbine performance and is carried out as:

$$W_{100} = W_{100,raw} \left(\frac{\rho_m}{1.225}\right)^{1/3} \tag{A.5}$$

$$\rho_m = \rho_d \left(\frac{1 + HUSS}{1 + 1.609 \times HUSS}\right) \tag{A.6}$$

$$\rho_d = \frac{PS}{\boldsymbol{R} \times (TAS + 273.15)} \tag{A.7}$$

[1] https://apps.ecmwf.int/codes/grib/param-db/?id=169

Eq.A.5 scales the wind speed $W_{100,raw}$ for air density as this affects the force exerted on the turbine blades, where ρ_m is the humidity corrected air density, which is in turn derived from the surface specific humidity ($HUSS$) as shown in eq.A.6. ρ_d is the dry air density which is derived using the ideal gas law from surface pressure [units-Pa](PS) and surface temperature (TAS) as shown in eq.A.7, where $\boldsymbol{R} = 287.058 Jkg^{-1}K^{-1}$ is the gas constant. $W_{100,raw}$ is calculated from the *100m u- and v- components of wind* from ERA5 data. Since ERA5 doesn't provide $HUSS$, we calculate it as (ref.[5]):

$$HUSS = \frac{0.622 \times VP}{0.01 \times PS - 0.378 \times VP} \tag{A.8}$$

$$VP = 6.112\, exp\left(\frac{17.67 \times TDPS}{TDPS + 243.5}\right) \tag{A.9}$$

where VP is the vapor pressure and $TDPS$ is the dewpoint temperature at surface in $^{\circ}C$(*2m temperature dewpoint temperature* in ERA5, converted from K to $^{\circ}C$).

Across WECC, few locations have wind speeds suitable for class I and II wind turbines based on the average wind speed over 2015-2020 from the ERA5 data (figure A.1). As a result, we estimate wind generation for all locations across WECC assuming a class-III wind turbine (provided in the source data 1 file). The power curve from SAM is provided as the power output at discrete wind speeds (figure A.2), and we convert this into a continuous function through linear interpolation using the interp1d function from the SciPy package. We include the discrete power curve in this SI.

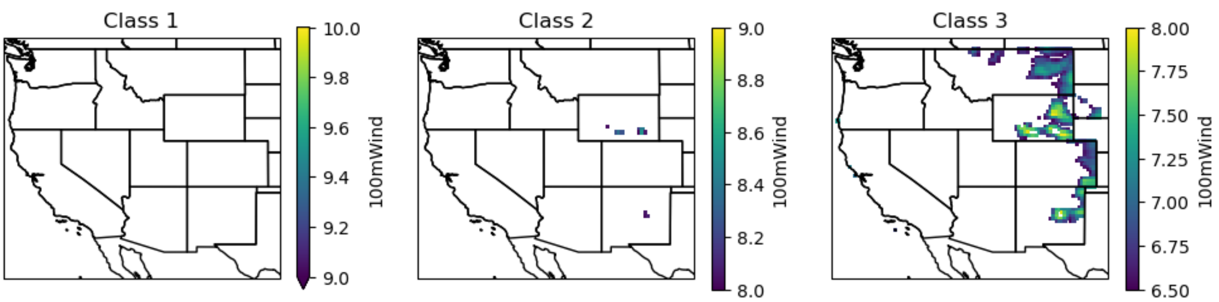

Figure A.1: Classification of geographical locations according to wind speed classes, based on 2015-2020 mean of 100m wind speeds

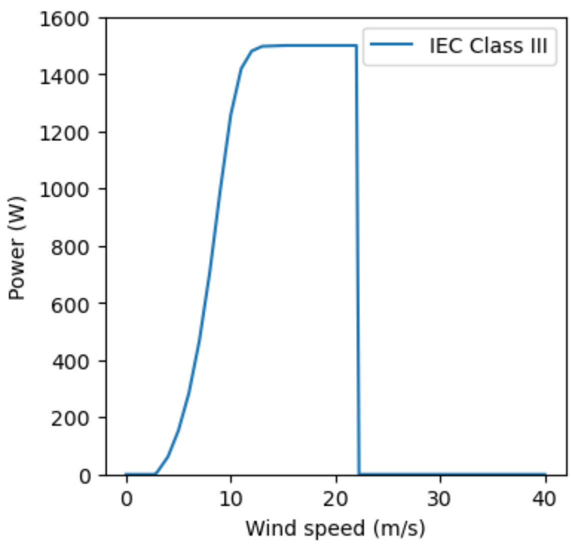

Figure A.2: Power curve for 1.5 MW IEC class III turbine

2 Capacity Expansion Model

The capacity expansion (CE) model optimizes new capacity investments, operations of new and existing units, and inter-regional electricity transfers by minimizing total system costs subject to system and unit-level constraints. Total system costs equal the sum of the cost of electricity generation of existing and new units and the

Parameter	Definition	Unit
P_c^{MAX}	Maximum power rating of new unit c	MW
$P_{c_s}^{EMAX}$	Maximum energy capacity of new storage unit c_s	MW
P_l^{MAX}	Maximum transmission capacity of line l	MW
FOM_c	Fixed O&M cost of new unit c	$/MW/year
OCC_c	Overnight capital cost of new unit c	$/MW
OCC_l	Overnight capital cost of transmission expansion along line l	$/MW
CRF_c	Capital recovery factor of new unit c	$/MW
CRF_l	Capital recovery factor of new transmission line l	$/MW
OC_c	Operational cost of new unit c	$/MWh
VOM_c	Variable O&M cost of new unit c	$/MWh
VOM_i	Variable O&M cost of existing unit i	$/MWh
OC_i	Operational cost of existing unit i	$/MWh
OC_c	Operational cost of new unit c	$/MWh
FC_c	Fuel cost of new unit c	$/MMBtu
FC_i	Fuel cost of existing unit i	$/MMBtu
HR_c	Heat rate of new unit c	MMBtu/MWh
HR_i	Heat rate of existing unit i	MMBtu/MWh
R	Discount rate = 0.07	–
LT_c	Life time of new units c	Years
N_c^{MAX}	Maximum number of new renewable units c built	Whole number
M	Planning reserve margin as fraction of peak demand	–
$D_{z,t}$	Total load (or electricity demand) in region z at time t	MWh
D_t	Total load (or electricity demand) across regions at time t	MWh

Table A.1: List of Parameters

cost of new capacity investments. Electricity generation costs equal the sum of fixed operations and maintenance (O&M) costs and variable electricity generation costs, which include fuel costs and variable O&M costs. The model runs till year 2030 in a 8 year increment to meet the prescribed renewable electricity (RE) penetration level for the US Western Interconnection (WECC). In each time step, the CE model can add any number of coal steam with carbon capture and sequestration (CCS), natural gas combined cycle (NGCC), NGCC with CCS, nuclear, wind, solar generators, battery and long-duration storage units, as well as DAC units and transmission line capacities.

2.1 Functional Forms

2.1.1 Parameters and Variables

Parameter	Definition	Unit
$P_{t,z}^{MAX,WIND}$	Maximum aggregate wind profile in region z at time t	MW
$P_{t,z}^{MAX,SOLAR}$	Maximum aggregate solar profile in region z at time t	MW
$H_{b,z}$	Maximum hydropower generation in region z and time block b	MWh
$Q_{i_s}^{MAX}$	Maximum charging rate of storage unit i_s	MW
$Q_{c_s}^{MAX}$	Maximum charging rate of new storage unit c_s	MW
$FOR_{i,t}$	Forced outage rate of existing unit i at time t	–
FOR_t^{RE}	Forced outage rate of existing wind and solar units at time t	–
$FOR_{c,t}$	Forced outage rate of new unit c at time t	–
RR	Renewable generation requirement as a fraction of total WECC-wide demand	–
$CF_{c_r,t}$	Capacity factor of new renewable unit c_r at time t	–
W_b	Scaling factor from number of representative to total hours in time block b	–
$X_{i_s}^{MAX}$	Maximum state of charge of existing storage unit i_s	MW
X_o	Initial state of charge as a fraction of maximum state of charge in each time block for existing and new storage units	–
RL_i	Maximum ramp rate of existing unit i	MW
RL_c	Maximum ramp rate of new unit c	MW
η	Round-trip efficiency of storage unit	%
ν	Transmission losses per unit of electricity transferred between regions	%

Table A.1: List of Parameters (Continued)

Set	Definition	Index	Note
$\mathbb{C}$	Set of potential new units	c	–
$\mathbb{C}_z$	Set of potential new units in region z	c_z	$\mathbb{C}_z \in \mathbb{C}$
$\mathbb{C}_r$	Set of potential new renewable units	c_r	$\mathbb{C}_r \in \mathbb{C}$
$\mathbb{C}_s$	Set of potential new storage units	c_s	$\mathbb{C}_s \in \mathbb{C}$
$\mathbb{C}_{s_z}$	Set of potential new storage units in region z	c_{s_z}	$\mathbb{C}_{s_z} \in \mathbb{C}_s$
$\mathbb{C}_{s'}$	Set of potential new non-storage units	$c_{s'}$	$\mathbb{C}_{s'} \in \mathbb{C}$
$\mathbb{I}$	Set of existing units	i	–
$\mathbb{I}_z$	Set of existing units in region z	i_z	$\mathbb{I}_z \in \mathbb{I}$
$\mathbb{I}_r$	Set of existing renewable units	i_r	$\mathbb{I}_r \in \mathbb{I}$
$\mathbb{I}_w$	Set of existing wind units	i_w	$\mathbb{I}_w \in \mathbb{I}$
$\mathbb{I}_{w_z}$	Set of existing wind units in region z	i_{w_z}	$\mathbb{I}_{w_z} \in \mathbb{I}_w$
$\mathbb{I}_o$	Set of existing solar units	i_o	$\mathbb{I}_o \in \mathbb{I}$
$\mathbb{I}_{o_z}$	Set of existing solar units in region z	i_{o_z}	$\mathbb{I}_{o_z} \in \mathbb{I}_o$
$\mathbb{I}_s$	Set of existing storage units	i_s	$\mathbb{I}_s \in \mathbb{I}$
$\mathbb{I}_{s_z}$	Set of existing storage units in region z	i_{s_z}	$\mathbb{I}_{s_z} \in \mathbb{I}_s$
$\mathbb{L}$	Set of transmission lines	l	–
$\mathbb{L}_z^{OUT}$	Set of transmission lines flowing out of region z	l_z^{OUT}	$\mathbb{L}_z^{OUT} \in \mathbb{L}$
$\mathbb{L}_z^{IN}$	Set of transmission lines flowing into region z	l_z^{IN}	$\mathbb{L}_z^{IN} \in \mathbb{L}$
$\mathbb{B}$	Set of time blocks	b	–
$\mathbb{T}$	Set of hours	t	–
$\mathbb{T}_p$	Set of peak demand hour	t_p	$\mathbb{T}_p \in \mathbb{T}$
$\mathbb{Z}$	Set of regions in WECC	z	–

Table A.2: List of Sets

Variable	Definition	Unit
n_c	Number of new units built of type c	Positive number
n_l	Total new transmission line capacity investments in line l	MW
k_{c_s}	Charge and discharge capacity built of new storage unit c_s	MW
e_{c_s}	State of charge capacity built of new storage unit c_s	MWh
$p_{i,t}$	Electricity generation (or electricity discharge) from existing unit i at time t	MWh
$p_{c,t}$	Electricity generation (or electricity discharge) from new unit c at time t	MWh
$f_{l,t}$	Total electricity flow in line l at time t	MWh
$q_{i_s,t}$	Electricity to charge existing storage unit i_s at time t	MWh
$q_{c_s,t}$	Electricity to charge new storage unit c_s at time t	MWh
$x_{i_s,t}$	State of charge of existing storage unit i_s at time t	MWh
$x_{c_s,t}$	State of charge of new storage unit c_s at time t	MWh

Table A.3: List of Variables

2.2 Objective Function

The CE model's objective function minimizes total annual fixed plus variable costs, where fixed costs capture investment costs in new transmission, electricity generators, and storage, and variable costs capture operational costs of new and existing generators:

$$
\begin{aligned}
TC^{CE} = & \left[\sum_{c_{s'}} n_{c_{s'}} \times P^{MAX}_{c_{s'}} \times \left(FOM_{c_{s'}} + OCC_{c_{s'}} \times CRF_{c_{s'}}\right)\right] \\
& + \left[\sum_{c_s} (k_{c_s} \times OCC_{c_s}) \times CRF_{c_s}\right] \\
& + \left[\sum_{l} n_l \times OCC_l \times CRF_l\right] + \left[\sum_{b} W_b \sum_{t_b \in T_b} \left(\sum_{c} p_{c,t_b} \times OC_c + \sum_{i} p_{i,t_b} \times OC_i\right)\right], \\
& \forall b \in \mathbb{B},\ i \in \mathbb{I},\ c \in \mathbb{C},\ c_{s'} \in \mathbb{C}_{s'},\ c_s \in \mathbb{C}_s, l \in \mathbb{L}
\end{aligned}
\tag{B.10}
$$

where c indexes potential new units, including both non-storage and storage units; $c_{s'}$ indexes potential new non-storage units; c_s indexes potential new storage units; b indexes time blocks; t indexes time intervals (hours); i indexes existing units; l indexes potential new transmission lines; n_c is number of new unit investments; n_l is total new transmission line capacity investments in line l (MW); P^{MAX} is maximum capacity of unit (MW); FOM is fixed operation and maintenance (O&M) costs of units (\$/MW/year); OCC is overnight capital cost of new investments (\$/MW); CRF is capital recovery factor; k is power rating of new storage units; W is scaling factor from number of representative to total hours in time block; p_c is electricity generation from new unit c (MWh); p_i is electricity generation from existing unit i (MWh); and OC is operational costs of new or existing units (\$/MWh). OC is defined for new and existing generators as:

$$OC_i = VOM_i + HR_i \times FC_i \qquad \forall i \in \mathbb{I}, \tag{B.11a}$$

$$OC_c = VOM_c + HR_c \times FC_c \qquad \forall c \in \mathbb{C} \tag{B.11b}$$

where VOM is variable O&M costs (\$/MWh), HR is heat rate (MMBtu/MWh), and FC is fuel cost (\$/MMBtu). CRF_c is defined as:

$$CRF_c = \frac{R}{1 - \dfrac{1}{(1+R)^{LT_c}}} \qquad \forall c \in \mathbb{C}, \tag{B.12}$$

where R is discount rate and LT is plant lifetime (years).

2.3 System-level Constraints

The CE model enforces a planning reserve margin, which requires total adjusted capacity to exceed peak annual demand across WECC:

$$
\begin{aligned}
(1+M) \times D_t \quad \leq \quad & \sum_{c_t \in C_t} P^{MAX}_{c_t} \times FOR_{c_t,t} \times n_{c_t} \\
& + \sum_{c_r \in C_r} P^{MAX}_{c_r} \times FOR_{c_r,t} \times n_{c_r} \times CF_{c_r,t} \\
& + \sum_{c_s \in C_s} FOR_{c_s,t} \times k_{c_s} \\
& + \sum_{i \in (I - I_W - I_O)} FOR_{i,t} \times P^{MAX}_i \\
& + \sum_{z} \left(P^{MAX,SOLAR}_{z,t} + P^{MAX,WIND}_{z,t}\right) \times FOR^{RE}_t, \\
& \forall t \in \mathbb{T}_p
\end{aligned}
\tag{B.13}
$$

where c_t and c_r index new thermal and renewable plant types, respectively; i_w and i_o index existing wind and solar generators, respectively; z indexes regions; M is a fraction of peak demand (equal to 0.13); FOR is forced outage rate; CF is capacity factor; $P^{MAX,SOLAR}$ is maximum regional generation by existing solar generators (MWh); $P^{MAX,WIND}$ is maximum regional generation by existing wind generators (MWh); and T_p indicates the annual peak demand hour. Adjusted capacity here accounts for temperature-dependent forced outage rates of generators [Table A.7] and hourly capacity factors for wind and solar facilities. Note that this PRM is enforced across all of WECC rather than on a region-by-region basis.

The CE model also requires supply balance demand at each time step:

$$\begin{aligned} D_{z,t} + \sum_{i_{s_z} \in \mathbb{I}_{s_z}} q_{i_{s_z},t} + \sum_{c_{s_z} \in \mathbb{C}_{s_z}} q_{c_{s_z},t} & \qquad \sum_{i_z \in \mathbb{I}_z} p_{i_z,t} + \sum_{c_z \in \mathbb{C}_z} p_{c_z,t} \\ + \sum_{l_z^{OUT} \in \mathbb{L}_z^{OUT}} f_{l_z^{OUT},t} & \leq \quad + \sum_{l_z^{IN} \in \mathbb{L}_z^{IN}} f_{l_z^{IN},t} \times \nu, \quad \forall z \in \mathbb{Z}, t \in \mathbb{T}, \end{aligned} \tag{B.14}$$

where z indexes zones, l indexes transmission lines, i_{s_z} indexes existing storage units in region z, c_{s_z} indexes new storage units in region z, i_z indexes existing units in region z, c_z indexes new units in region z, l_z^{IN} indexes lines flowing out of region z, l_z^{OUT} indexes transmission lines flowing out of region z, q is the electricity used to charge storage units (MWh), ν indicates losses for each unit of electricity imported into a region (assumed to be 5%), and f is electricity flows along transmission lines.

The total electricity flow through a transmission line ($f_{l,t}$) cannot exceed the line's initial transmission capacity (P_l^{MAX}) plus new capacity investments (n_l):

$$f_{l,t} \leq P_l^{MAX} + n_l, \quad \forall l \in \mathbb{L},\ t \in \mathbb{T}, \tag{B.15}$$

where l indexes transmission lines, and $f_{l,t}$ is total electricity flow in line l at time t (MWh).

To examine power systems with increasing renewable penetrations, we constrain wind and solar generation to be greater than or equal to a percentage of total electricity demand:

$$\sum_{t,c_r} p_{c_r,t} + \sum_{t,i_r} p_{i_r,t} \geq \sum_{t,z} P_{z,t}^D \times RR, \quad \forall t \in \mathbb{T},\ c_r \in \mathbb{C}_r, i_r \in \mathbb{I}_r, z \in \mathbb{Z} \tag{B.16}$$

where RR equals the renewables requirement as a fraction of total demand. We enforce this constraint at the WECC-level.

2.4 Unit-level Constraints

2.4.1 Investment constraints

The CE model places an upper bound on wind and solar investments by grid cell based on the area of each grid cell and the energy density of wind and solar:

$$0 \leq n_{c_r} \times P_{c_r}^{MAX} \leq N_{c_r}^{MAX}, \quad \forall c_r \in \mathbb{C}_r \tag{B.17}$$

where n_{c_r} equals investment in new wind or solar plants. Maximum wind and solar investment per grid cell equals 8.8 and 55.5 GW, respectively, using densities of 0.9 and 5.7 W/m^2 [6] and the approximate area of 961 km^2 corresponding to a 0.25 Degree latitude x 0.25 Degree longitude grid cell.

2.4.2 Generation constraints

For existing generators, electricity generation is limited by the generators' capacities:

$$0 \leq p_{i,t} \leq P_i^{MAX}, \quad \forall t \in \mathbb{T},\ i \in \mathbb{I} \tag{B.18}$$

Combined electricity generation by existing wind and solar generators is limited to aggregate wind and solar generation profiles:

$$\sum_{i_{w_z} \in \mathbb{I}_{w_z}} p_{i_{w_z},t} \leq P_{z,t}^{MAX,WIND}, \quad \forall t \in \mathbb{T}, z \in \mathbb{Z}, \tag{B.19a}$$

$$\sum_{i_{o_z} \in \mathbb{I}_{o_z}} p_{i_{o_z},t} \leq P_{z,t}^{MAX,SOLAR}, \quad \forall t \in \mathbb{T}, z \in \mathbb{Z}, \tag{B.19b}$$

New generators' electricity generation cannot exceed their new capacity investments:

$$0 \leq p_{c,t} \leq n_c \times P_c^{MAX}, \quad \forall t \in \mathbb{T},\ c \in \mathbb{C} \tag{B.20}$$

Electricity generation by new renewable generators is also constrained by site-specific capacity factor time-series:

$$p_{c_r,t} \leq n_{c_r} \times P_{c_r}^{MAX} \times CF_{c_r,t}, \quad \forall t \in \mathbb{T},\ c_r \in \mathbb{C}_r \tag{B.21}$$

Hydropower generation is constrained based on observed data for each of our weather years. Since we ignore transmission constraints within each of our five regions, we aggregate hydropower capacity by region, then limit total hydropower generation by time block:

$$\sum_{t_b \in T_b, i_{h_z} \in I_{h_z}} p_{i_{h_z},t_b} \leq H_{b,z}, \forall z \in \mathbb{Z}, b \in \mathbb{B} \tag{B.22}$$

where i_{h_z} indexes all hydropower units in region z and $H_{b,z}$ equals maximum toal hydropower generation in time block b and region z [2.6.2].

The CE model places an upper bound on upwards changes in electricity generation from one time period to the next, i.e. in upward ramps, for new and existing units:

$$p_{i,t_b} - p_{i,t_b-1} \leq RL_i, \quad \forall t_b > 1, i \in \mathbb{I} \tag{B.23a}$$

$$p_{c,t_b} - p_{c,t_b-1} \leq n_c \times P_c^{MAX} \times RL_c \quad \forall t_b > 1, c \in \mathbb{C} \tag{B.23b}$$

where RL equals the ramp limit. We only constrain upwards ramps for two reasons: (1) downward ramps can be more easily achieved through curtailment of renewables than upwards ramps and (2) for computational tractability. Ramping constraints for new and existing generators are enforced between time periods within each time block, but not between time blocks.

2.4.3 Storage constraints

The energy capacity of storage built of (e_{c_s}) is constrained to a fixed energy to power ratio ($P_{c_s}^{EMAX}/P_{c_s}^{MAX}$) times invested power capacity:

$$0 \leq e_{c_s} \leq \frac{P_{c_s}^{EMAX}}{P_{c_s}^{MAX}} k_{c_s}, \quad \forall c_s \in \mathbb{C}_s \tag{B.24}$$

For storage units (i_s, c_s), state of charge (SOC) (x (MWh)) depends on the prior period's state of charge, electricity discharge (p (MWh)), and energy inflow (or charging) (q (MWh)) while accounting for round-trip efficiency (η) losses:

$$0 \leq x_{i_s,t} = x_{i_s,t-1} - 1/\sqrt{\eta} \times p_{i_s,t} + \sqrt{\eta} \times q_{i_s,t} \leq X_{i_s}^{MAX}, \quad \forall t > 1, i_s \in \mathbb{I}_s \tag{B.25a}$$

$$0 \leq x_{c_s,t} = x_{c_s,t-1} - 1/\sqrt{\eta} \times p_{c_s,t} + \sqrt{\eta} \times q_{c_s,t} \leq e_{c_s}, \quad \forall t > 1, c_s \in \mathbb{C}_s \tag{B.25b}$$

We assume 81% round-trip efficiency for all storage units.

In hour 1, the state of charge is assume to equal to a fixed fraction (X_o) of the maximum state of charge:

$$x_{i_s,t=1} = X_0 \times X_{i_s}^{MAX}, \quad \forall i_s \in \mathbb{I}_s \tag{B.26a}$$
$$x_{c_s,t=1} = X_0 \times e_{c_s}, \quad \forall c_s \in \mathbb{C}_s, \tag{B.26b}$$

where X_0 is the initial SOC fraction.

Charging and discharging are limited by max discharge and charge rates, which for new generators are decision variables noted above, and must be greater than zero:

$$p_{i_s,t} \leq P_{i_s}^{MAX}, \quad \forall i_s \in \mathbb{I}_s, t \in \mathbb{T} \tag{B.27a}$$
$$p_{c_s,t} \leq k_{i_s}, \quad \forall c_s \in \mathbb{C}_s, t \in \mathbb{T} \tag{B.27b}$$
$$0 \leq q_{i_s,t} \leq Q_{i_s}^{MAX}, \quad \forall i_s \in \mathbb{I}_s, t \in \mathbb{T} \tag{B.27c}$$
$$0 \leq q_{c_s,t} \leq k_{i_s}, \quad \forall c_s \in \mathbb{C}_s, t \in \mathbb{T} \tag{B.27d}$$

where $Q_{i_s}^{MAX}$ equals the maximum charging rate of storage assets, which we set equal to $P_{i_s}^{MAX}$.

Discharging cannot exceed the prior period's state of charge:

$$p_{i_s,t} \leq x_{i_s,t-1} \quad \forall i_s \in \mathbb{I}_s, t > 1 \tag{B.28a}$$
$$p_{c_s,t} \leq x_{c_s,t-1} \quad \forall c_s \in \mathbb{C}_s, t > 1 \tag{B.28b}$$

2.5 Model Solutions

The CE model solution determines new investments in generators, storage, and transmission assets by region or (in the case of wind and solar) grid cell; hourly electricity generation of new and existing units; hourly discharging, charging and states of charge of storage units; and electricity flows between regions. These solutions result from solving the optimization model described above with objective function B.10 subject to all constraints listed above [B.13,B.14,B.16,B.17,B.18,B.19,B.20,B.21,B.22,B.23a,B.24,B.25,B.26,B.27,B.28].

2.6 Data

In this section, we discuss the data and intermediate steps to calculate the parameters that are used in the model.

2.6.1 Regional Demand for Electricity

The sub-regional loads are constructed by aggregating loads in smaller balancing authorities located within their boundaries. Table

Sub-region	Balancing Authorities aggregated to find demand
CAMX	CISO, BANC, TIDC, LDWP
Desert Southwest	IID, AZPS, SRP, EPE, PNM, TEPC, WALC
NWPP Central	NEVP, PACE, IPCO, PSCO
NWPP NE	WACM, NWMT, WAUW, PACE
NWPP NW	PSEI, DOPD, CHPD, AVA, TPWR, GCPD, BPAT, PGE, PACW, SCL

Table A.4: Sub-region – balancing authority mapping to obtain aggregate demand

2.6.2 Generator Fleet

Initial Generator Fleet To construct our 2020 initial representative existing generator fleet, we begin with unit-level data on active existing units from *The National Electric Energy Data System* (NEEDS) dataset version 6 (updated in June 2020) (accessed 10/02/2021) [7]. Because NEEDS lacks storage unit parameters and other parameters need in our CE model, we merge the NEEDS dataset with EIA860 dataset [8] and add carbon dioxide (CO_2) emission rates from the the U.S. Energy Information Administration (EIA)'s *Carbon Dioxide Emissions Coefficients* [9], fuel prices from EIA's *Annual Energy Outlook 2020, Table 3. Energy Prices by Sector and Source* [10], and variable operation and maintenance (O&M) costs from [11]. We isolate generators within WECC, our study region, using shape files of balancing areas within WECC from NREL's ReEDS model [12]. Our initial generator fleet is described in the table A.5. The *other* type of generators in the table below include geothermal, different types of waste, biomass, and other small fossil generators, which are all modeled as dispatchable capacity in the CEM and RAM.

Sub-region	Combined cycle gas	Simple cycle gas	Hydro	Nuclear	Steam turbine coal	Solar	Storage	Wind	Other
CAMX	20641	10825	10147	0	17	10644	3660	5764	4010
Desert Southwest	11256	4855	3840	3937	5333	2303	287	1488	363
NWPP Central	10486	5053	954	0	6693	3128	670	3636	1045
NWPP NE	94	465	3493	0	6562	40	0	2906	23
NWPP NW	6619	1669	32091	1180	0	356	364	6568	557

Table A.5: Initial generator fleet capacity of each generator type (in MW) across the subregions

Hydropower Generation In the CEM, we dispatch hydropower generation on a regional hourly basis as an energy-limited resource [ref eq. B.22]. Energy limits are defined for each time block using historic, weather-year-specific generation from Form EIA-923. We estimate monthly historic generation for each weather year by matching hydropower ORIS plant codes between our initial generator fleet and Form EIA-923. We then convert monthly generation to a total energy budget for each time block modeled in the CEM (4 representative blocks per season and 1 day for peak annual demand, net demand, and 1-hour upward ramp). This conversion happens in two steps. First, we divide monthly to hourly hydropower generation budgets using the proportion of monthly to hourly net demand. In some cases, this results in hours with generation exceeding regional hydropower capacity. For these hours, we iteratively reallocate surplus hourly generation to other hours using the proportion of monthly to hourly net demand, until regional hydropower generation does not exceed regional capacity in any hour. Finally, we sum hourly hydropower generation for all hours included in each time block.

Generator Fleet Compression Because the existing generation fleet in WECC is large with over 4,500 units, we combine (or aggregate) existing small generators into larger generators for computational tractability. We aggregate generators within the same region using two steps and several criteria. First, for each fuel type and plant type with zero marginal costs, we aggregate all generators into a single generator by region. Zero marginal cost generators include all geothermal, wind, solar, landfill gas, municipal solid waste, biomass, and non-fossil waste generators. Second, for each fuel type and plant type with non-zero marginal costs, we aggregate generators based on age and heat rate to preserve heterogeneity in operational costs. These non-zero marginal cost units include distillate fuel oil, natural gas combined cycle, natural gas combustion turbine, residual fuel oil, and coal (including bituminous, sub-bituminous, and lignite) generators. Specifically, by region, plant type, and fuel type, we divide generators into 4 heat rate blocks, then aggregate generators together within each heat rate block by decade between 1975 and 2026. We aggregate generators up to 200 MW in size in this manner, and create combined generators of up to 10,000 MW. These size thresholds significantly reduce the size of the generator fleet while still individually modeling mid- to large-sized power plants. Heat rates and CO_2 emission rates of the aggregated generators equal the capacity-weighted heat rates and CO_2 emission rates of their constituent generators.

2.6.3 Generator Investment Options

The CE model determines generator additions of three plant types: wind, solar PV, and 4-hour utility-scale battery storage. We obtain overnight capital costs and fixed and variable operation and maintenance (O&M) costs from NREL's Annual Technology Baseline (ATB) moderate technology development scenario for 2030 [11]. For computational tractability, we remove the lowest 40% of possible wind and solar investment locations in each region (i.e., grid cells) based on average annual capacity factor prior to running our CEM, leaving us with roughly 3,000 wind & solar locations across WECC.

2.6.4 System Topology

Our resource adequacy (RA) model uses the five regions that WECC uses to quantify resource adequacy in WECC [13]: NWPP NW, NWPP NE, CAMX, Desert Southwest, and NWPP Central [see figure A.3]. To align regions between the CE and RA models, we model these same five regions in our CE model.

Within each of these regions, we ignore transmission constraints. Between regions, we enforce transmission constraints. Given the lack of data regarding transmission constraints between our WECC resource adequacy regions, we estimate inter-regional transmission constraints using data from the National Renewable Energy Laboratory (NREL) Regional Energy Deployment System (ReEDS) model. ReEDS provides transmission constraints between 35 balancing areas across WECC. We assign each balancing area to a region using spatial overlays, then set transmission constraints between each pair of regions as the sum of transmission constraints between each pair of balancing areas within each region. Using this method, we identify seven inter-regional, bi-directional transmission constraints. For each of these seven inter-regional transmission constraints, we limit hourly inter-regional electricity transfers to an upper capacity bound.

In addition to enforcing existing transmission constraints, the CE model can also invest in new transmission capacity between each of the seven inter-regional transmission interfaces identified above. Similar to other macro-scale planning models [14], we assume costs scale linearly with new transmission capacity, allowing us to maintain a computationally tractable linear program (LP). Per-MW costs of transmission expansion equal the distance (in miles) between the two centroids of interconnected regions times the per MW-mile cost of each bi-directional transmission line. We estimate this cost as the median of costs between each pair of balancing authorities between regions, which is taken from NREL's ReEDS Model's open access github [12]. Table A.6 depicts all possible combinations of aggregate links between our five load regions and their respective aggregate capacities and total cost per MW.

2.7 WECC subregions

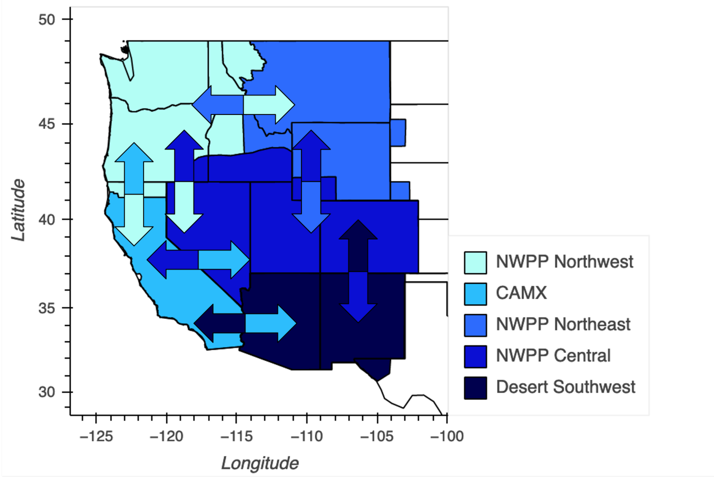

Figure A.3: WECC subregions used in the CEM and RAM. Arrows show transmission flows between the subregions.

Transmission Capacity between	Total Capacity (GW)	Expansion Cost (1000$/MW)
NWPP-NW and NWPP-NE	12.3	474
NWPP-NW and CAMX	7.1	1,018
NWPP-NW and NWPP-Central	1.5	569
NWPP-NE and NWPP-Central	6.0	431
CAMX and Desert Southwest	3.0	1,070
CAMX and NWPP-Central	4.6	816
Desert Southwest and NWPP-Central	5.6	348

Table A.6: Transmission Networks within WECC

2.8 Model Code and Data Availability

CEM code and data are available at `https://github.com/atpham88/US-CE`.

3 Resource adequacy model

3.1 Transmission between sub-regions

The transmission energy balance between the WECC subregions is modelled as a simple network flow problem without accounting for direction of flow in the circuit. For each iteration and each hour where there is a deficit in any sub-region, this flow problem is solved as a linear program.

3.1.1 Objective

The objective is to minimize the cost of transmission flow and cost of energy not served.

$$\begin{aligned} \min_{f,ens} \quad \sum_{i} \quad [T_c \times (\sum_{j,j\neq i} f_{ij}) + ENS_c \times e_i] \\ \forall\, i,j \in [1,N] \end{aligned} \tag{C.29}$$

Where N is the number of sub-regions (henceforth referred to as nodes), f_{ij} is the unidirectional flow from node i to j, and e_i is energy not served or energy deficit at each node, T_c and ENS_c are the line transmission and energy not served cost (both $\$/MWh$).

3.1.2 Constraints

$$\begin{aligned} &\sum_{j,j\neq i} (f_{ij} - f_{ji}) - e_i \leq R_i \quad \forall\, i \in [1,N] \\ &0 \leq f_{ij} \leq F_{ij}, \quad e_i \geq 0 \quad \forall\, i,j \in [1,N] \end{aligned} \tag{C.30}$$

where $R_i \in \mathbb{R}$ is the residual or net load in each node and F_{ij} is the flow limits on each transmission line. When the residual is positive the node can export and when the residual is negative the transfers into the region is positive or there is unserved energy.

3.2 RAM iteration convergence

Figure A.4 provides the LOLH, EUE, and simulation time across 25 simulations for 250 and 500 Monte Carlo iterations for the weather year 2017 and 45% RE penetration scenario. As the iteration size increases, the distribution of LOLH estimates tightens. Increasing iterations results in narrowing of the LOLH distribution, with similar range in EUE, but increases computation time by more than 3x. For other weather years and RE scenarios, the simulation times is much higher, for instance, with RE=45% and 2019 weather year, this simulation takes around 4 hours to complete. Since we are more interested in the timing of the risk hours and not amount of risk throughout our analysis, this variation in LOLH does not impact our findings.

3.3 Forced outage rate

Table A.7 shows the outage probabilities of the various generators as a function of ambient temperature.

Table A.7: Temperature dependent forced outage rates of different generators

Closest temperature value [$^{\circ}C$]	-15	-10	-5	0	5	10	15	20	25	30	35
Nuclear	1.9 %	1.8 %	1.7 %	1.8 %	1.9 %	2.1 %	2.7 %	3.1 %	3.9 %	6.6 %	12.4 %
Combined cycle gas	14.9 %	8.1 %	4.8 %	3.3 %	2.7 %	2.5 %	2.8 %	3.5 %	3.5 %	4.1 %	7.2 %
Simple cycle gas	19.9 %	9.9 %	5.1 %	3.1 %	2.4 %	2.2 %	2.4 %	2.7 %	3.1 %	3.9 %	6.6 %
Steam turbine coal	13.3 %	11.2 %	9.9 %	9.1 %	8.6 %	8.3 %	8.4 %	8.6 %	9.4 %	11.4 %	14. %
Hydro	7 %	4.3 %	3.2 %	2.7 %	2.6 %	2.6 %	2.7 %	2.7 %	2.5 %	2.9 %	8.2 %
Solar, wind, storage, other	5 %	5 %	5 %	5 %	5 %	5 %	5 %	5 %	5 %	5 %	5 %

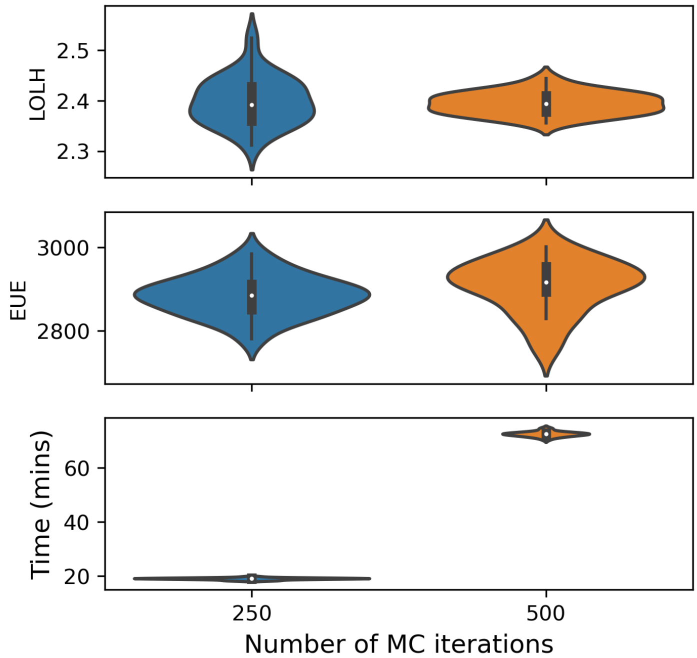

Figure A.4: Variation in range of LOLH with increasing number of Monte Carlo samples

4 Self organizing maps and Weather Patterns

To test the sensitivity of the SOM technique to grid size and training iterations for identifying weather regimes (WR), we use the metrics quantization error (QE) and topographic error (TE) [15]. QE represents the variance within the SOM node and is calculated as the L2 error between the daily circulation maps assigned to a node and the node centroid. TE represents the continuity in the map. TE is calculated by finding the fraction of inputs for which the best matching node (the node it is assigned to) and the second best matching node are not neighboring WRs. So, we want to minimize QE to make the node centroid (weather pattern for our purposes) more representative of the maps assigned to it and minimize TE to ensure the map nodes are topologically continuous. Figure A.5a shows how QE and TE vary for different grid shapes used to train the SOM. We find that a 3x3 grid produces a map that best balances QE and TE. Figure A.5b shows the sensitivity of QE and TE to training iterations. We find 1000 or 5000 iterations is optimal to minimize both QE and TE. Though 1000 iterations does marginally better in comparison to 5000 iterations, we get more stable maps when retraining using 5000 iterations, hence use that to obtain our weather patters.

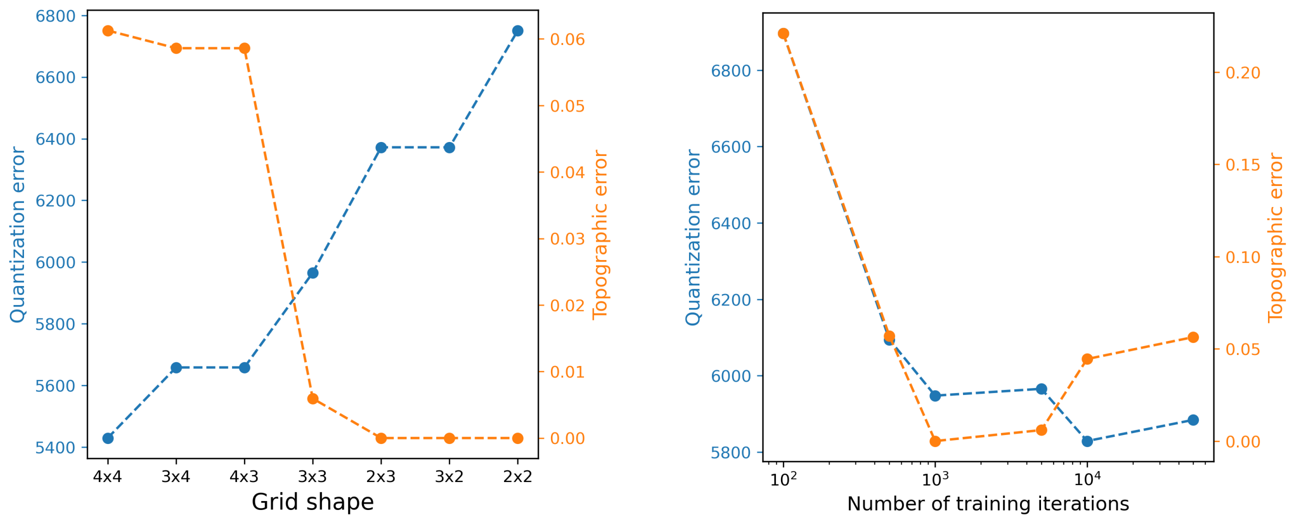

(a) **(b)**

Figure A.5: Quantization and topographic error for different (a) grid shapes of the SOM (row x columns) (b) training iterations

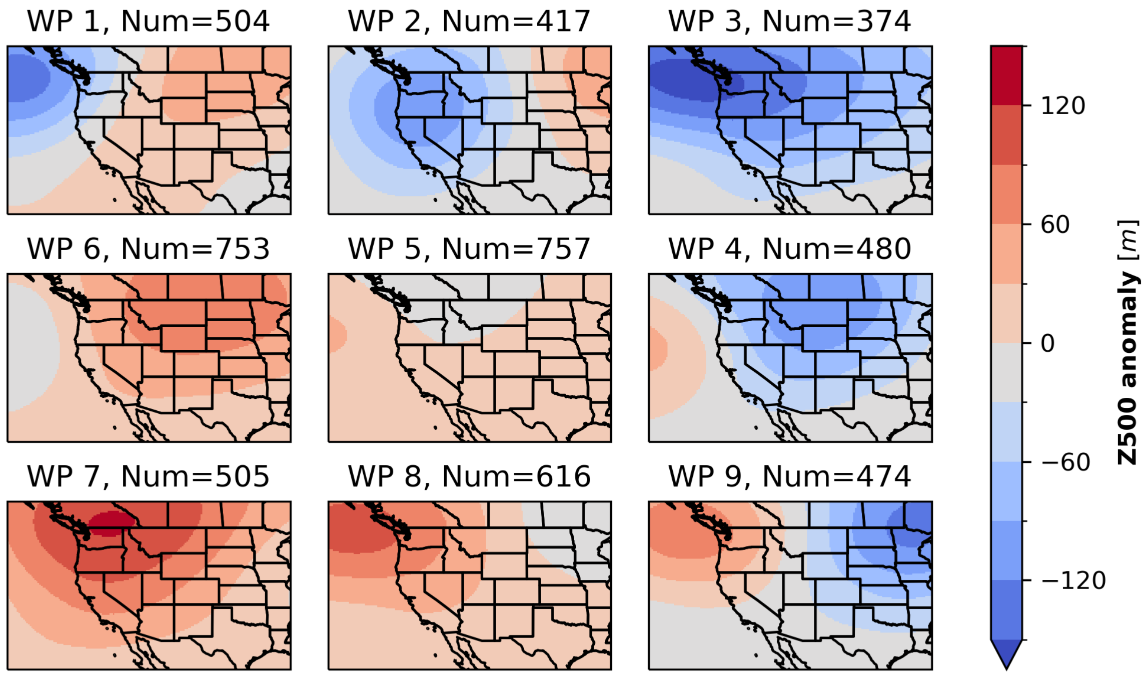

Figure A.6: Weather patterns representing the weather regimes with the titles for each panel indicating the number of extended summer days from June-September from 1981-2020 that fall into each weather regime

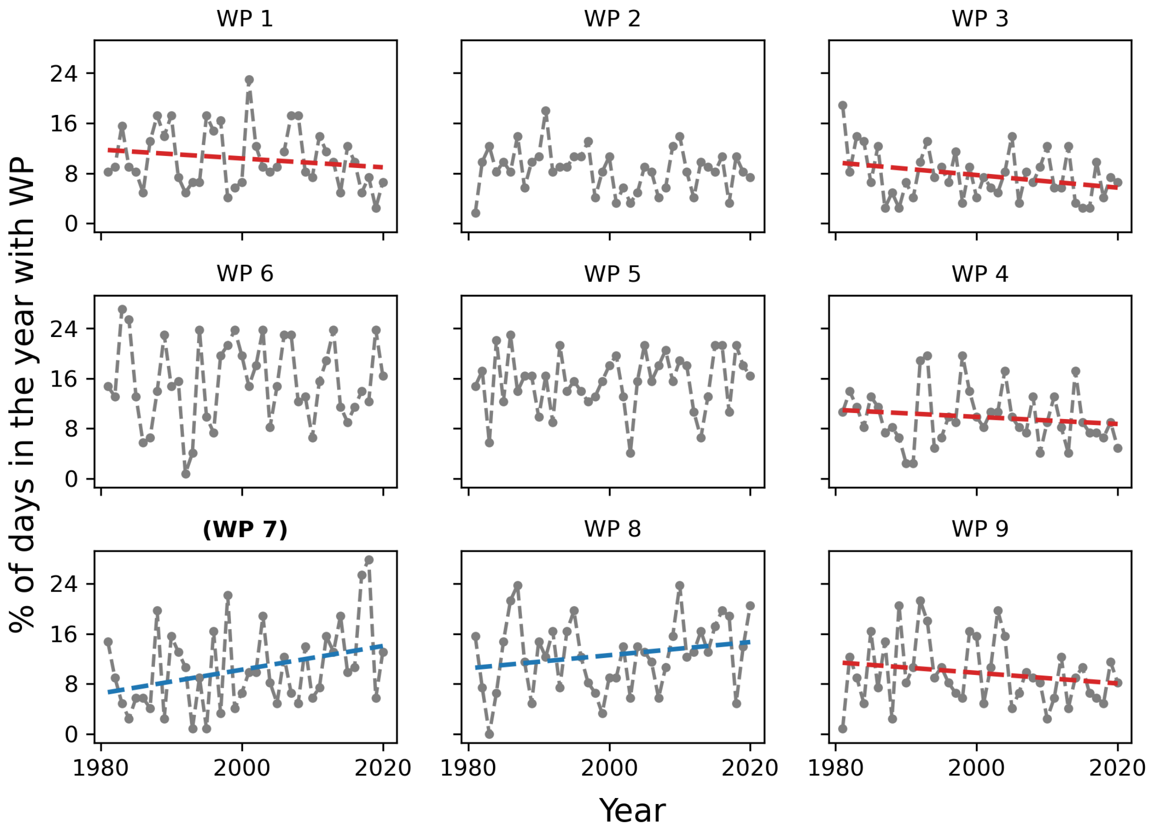

Figure A.7: Grey dots show the percentage of extended summer days from 1981 - 2020 belonging to each weather regime. Red (negative slope) and blue (positive slope) dotted lines show a linear regression if the trend is greater than or equal to —0.05— and bold parenthesized text indicates a 95% statistical significance of regression coefficient

5 Results SI

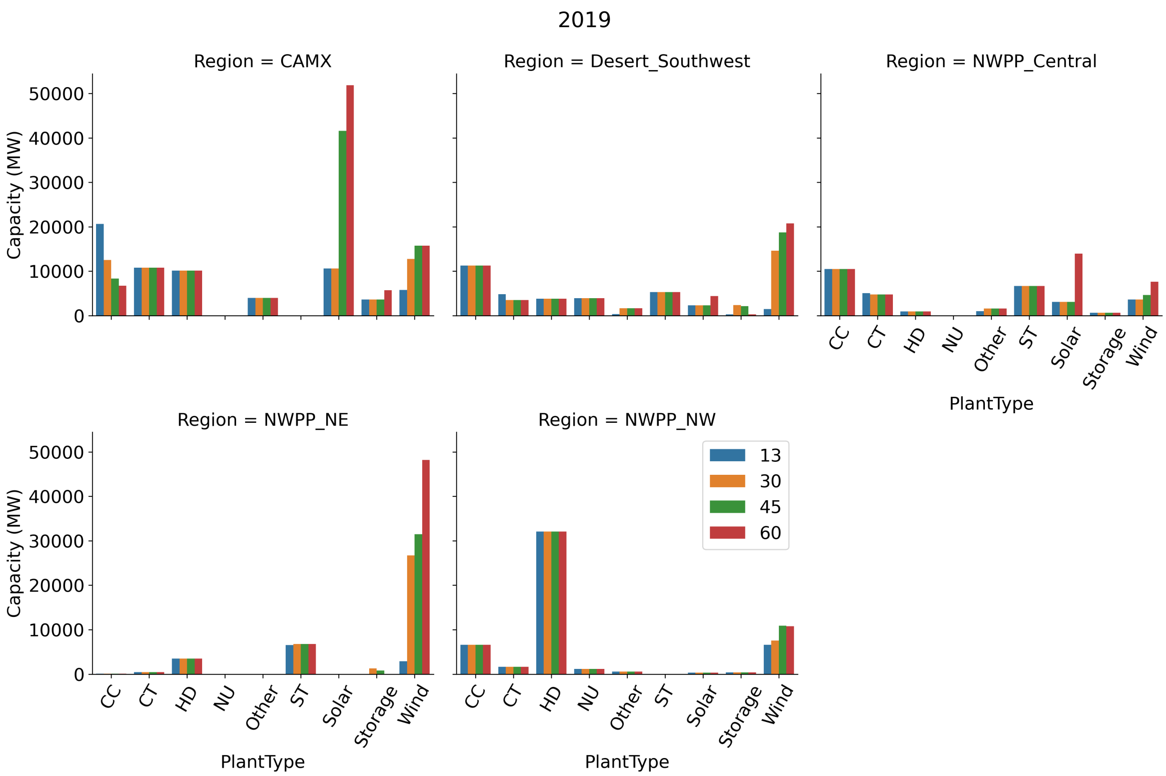

Figure A.8: For the 2019 weather year this figure shows installed capacities of different generation sources in the subregios with increasing renewable penetrations.

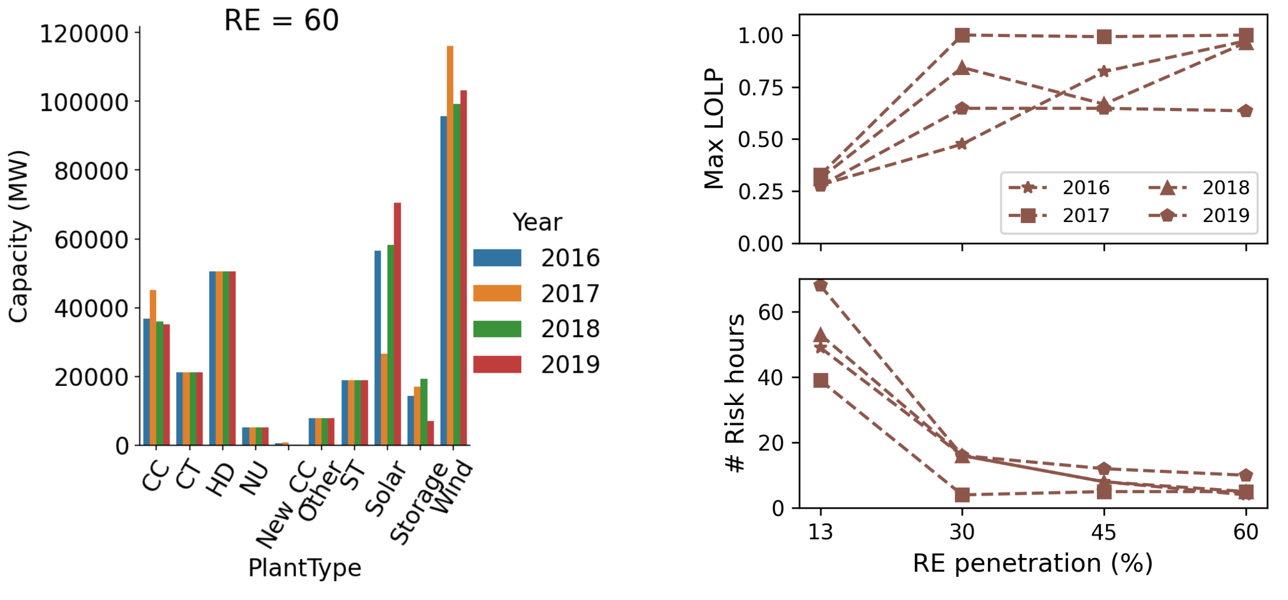

(a) **(b)**

Figure A.9: (a) Installed capacity of different generation assets across the weather years with at 60% RE penetration; (b) Max LOLP (top) and number of risk hours (bottom) across the weather years with increasing RE generation levels;

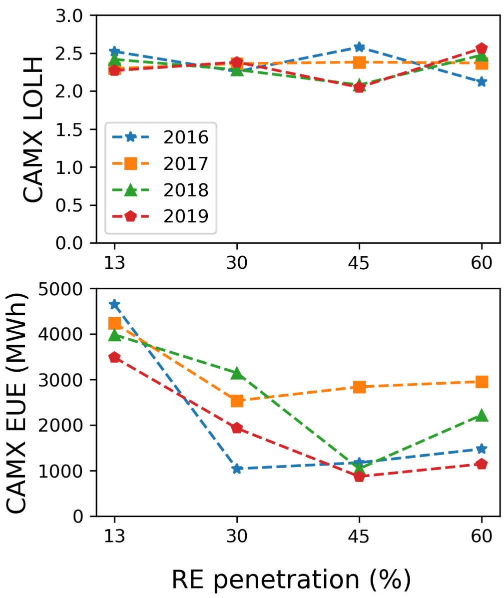

Figure A.10: LOLH and EUE across the weather years with increasing RE generation levels

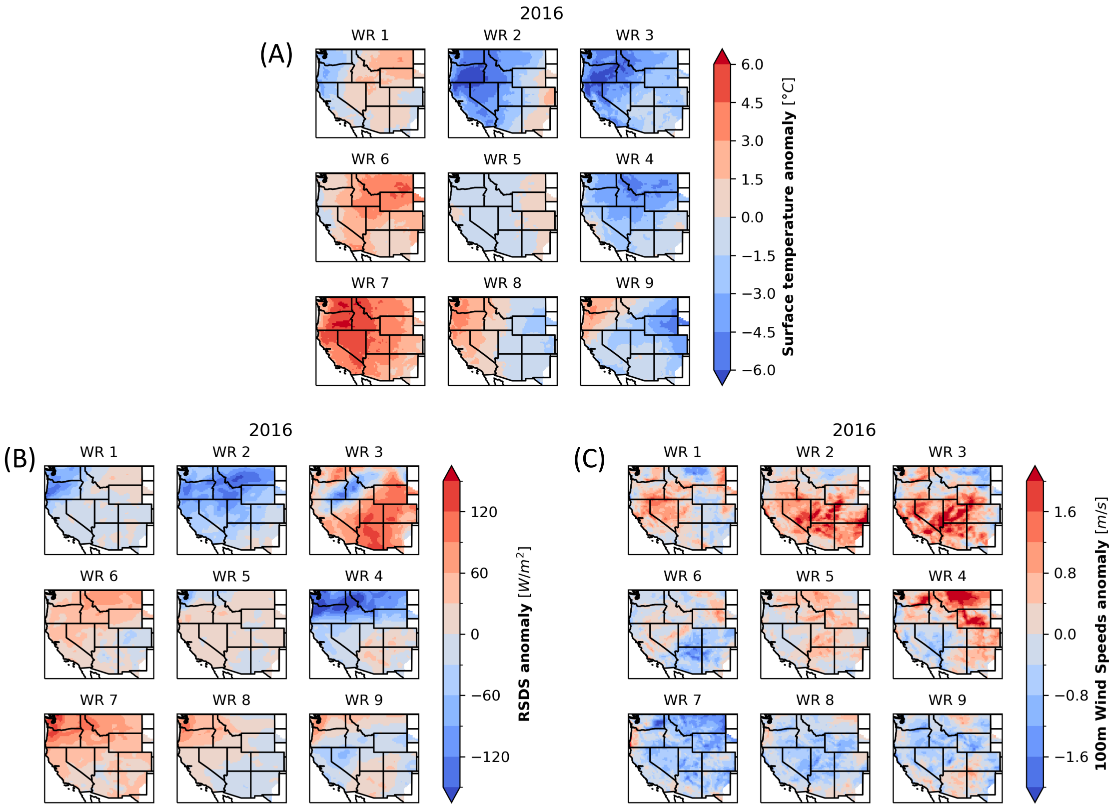

Figure A.11: Composites of surface temperature (A), surface solar radiation (B), and 100m wind speeds (C) anomalies. The composites are constructed based on the hours from 2016 extended summer belonging to each weather regime.

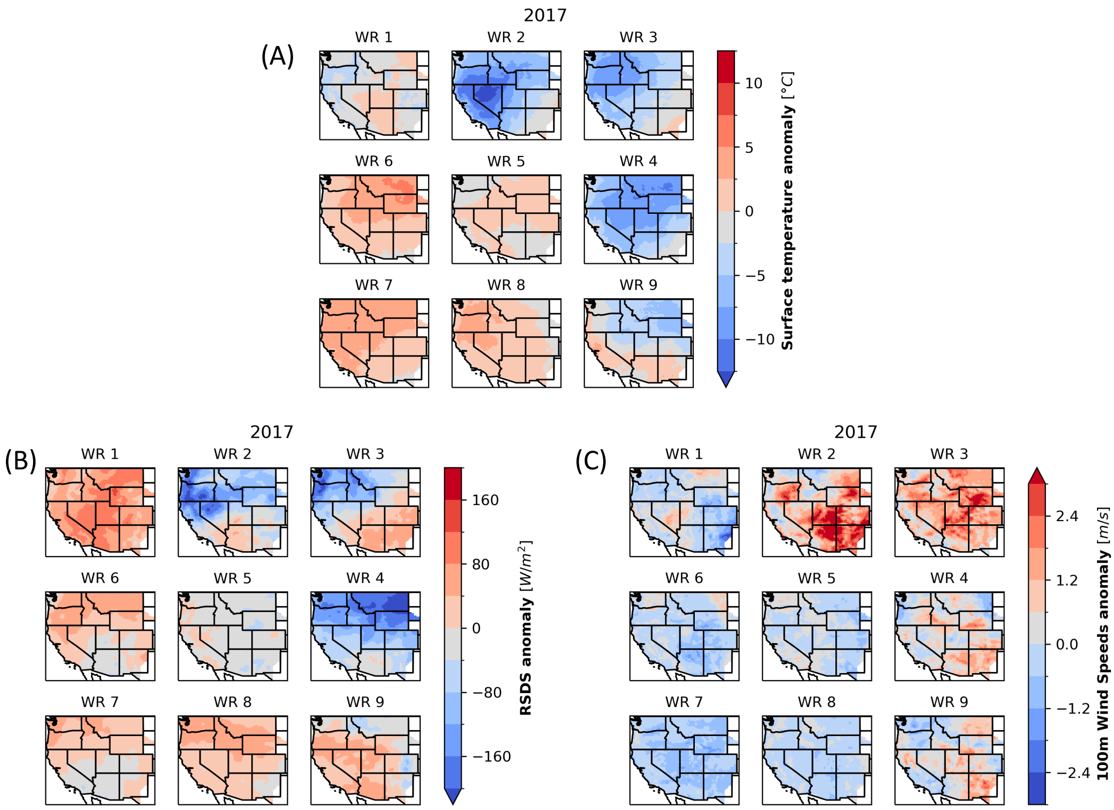

Figure A.12: Composites of surface temperature (A), surface solar radiation (B), and 100m wind speeds (C) anomalies. The composites are constructed based on the hours from 2017 extended summer belonging to each weather regime.

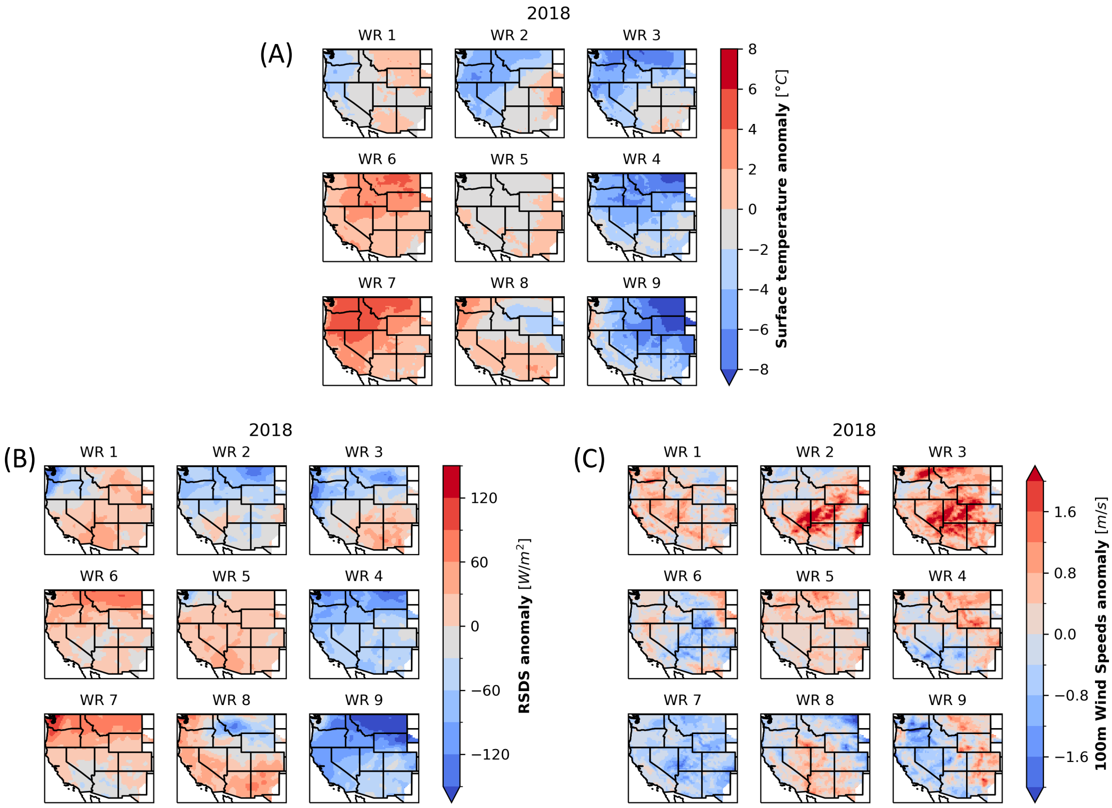

Figure A.13: Composites of surface temperature (A), surface solar radiation (B), and 100m wind speeds (C) anomalies. The composites are constructed based on the hours from 2018 extended summer belonging to each weather regime.

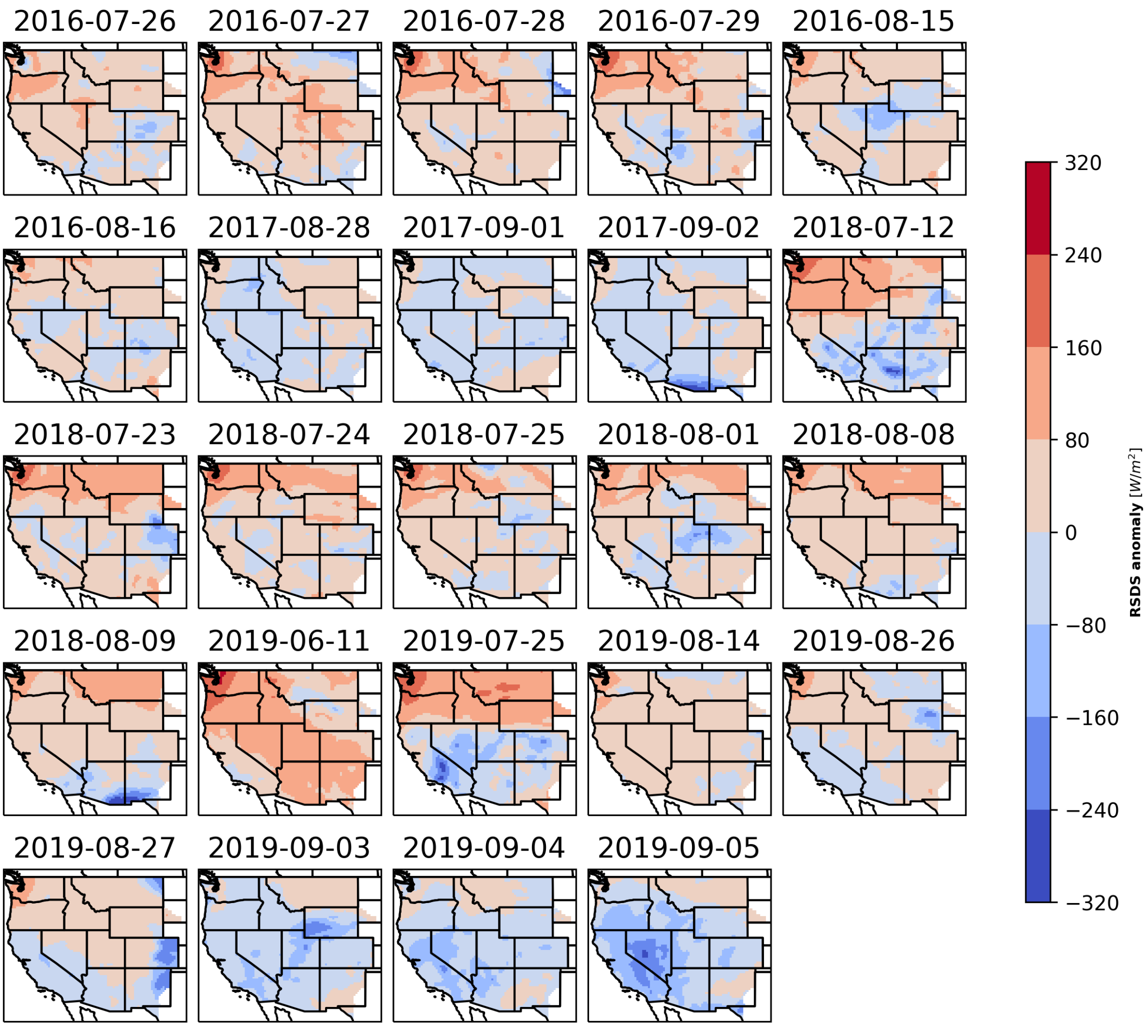

Figure A.14: Daily surface solar radiation anomalies on days with RA failure events for RE penetrations from 30% to 60% across the weather years.

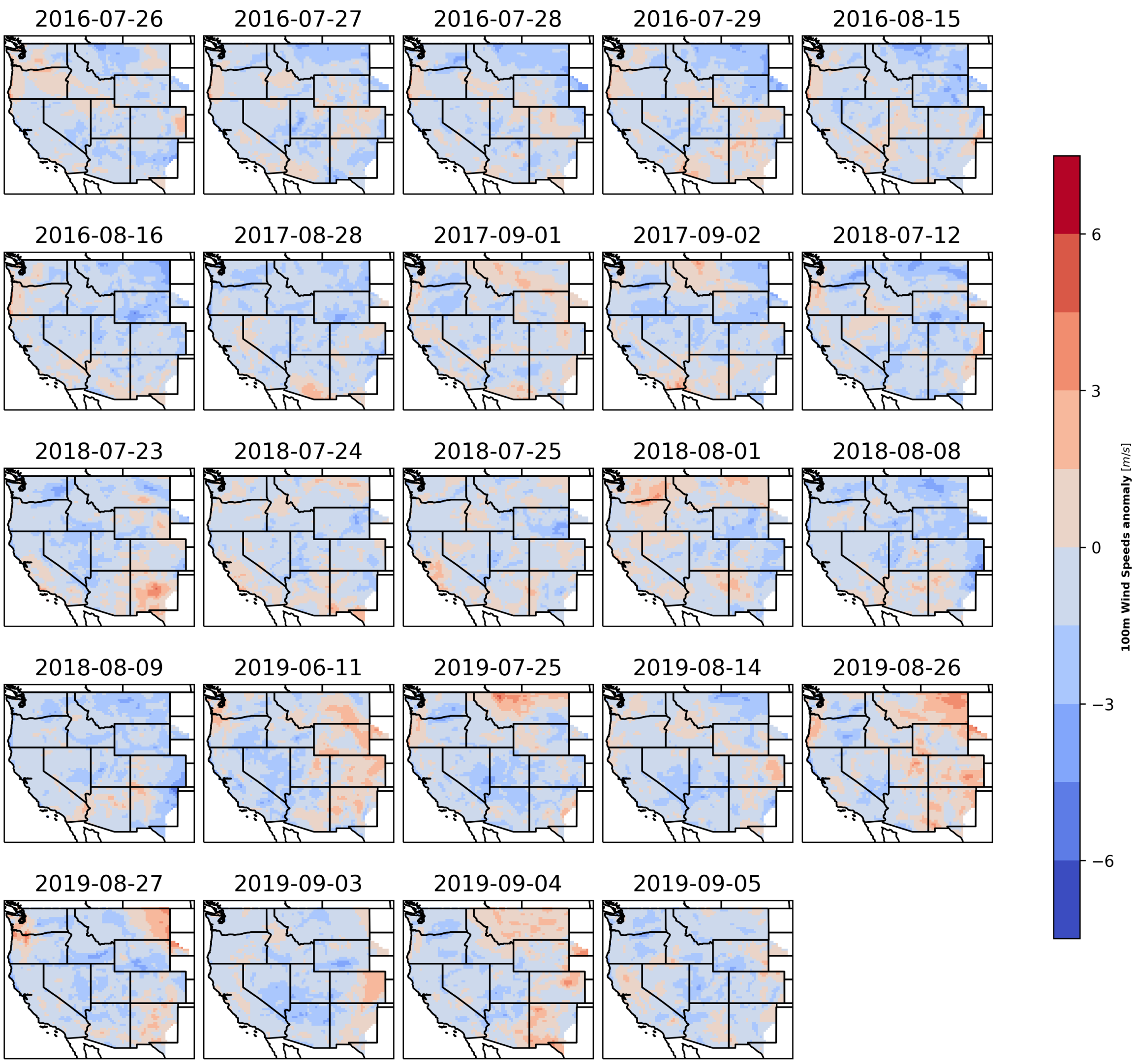

Figure A.15: Daily 100m wind speeds anomalies on days with RA failure events for RE penetrations from 30% to 60% across the weather years.

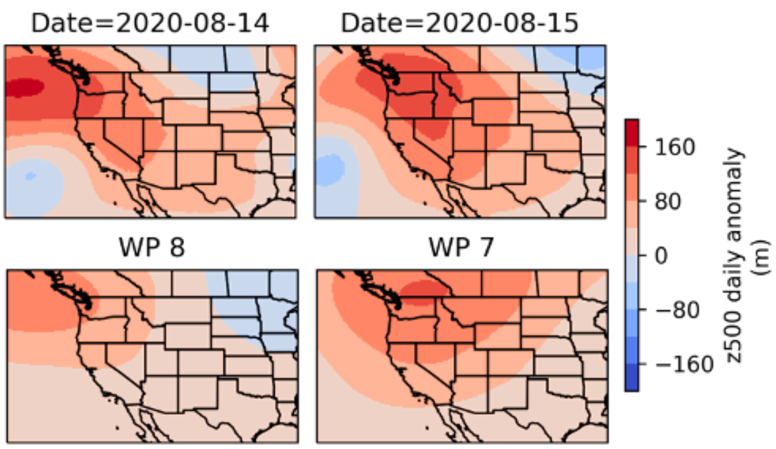

Figure A.16: Daily Z500 anomaly on August 14th and 15th 2020 (Top panels) and WPs 8 and 9 from the extended summer weather regimes (Bottom panels).

References

[1] Sonia Jerez, Isabelle Tobin, Robert Vautard, Juan Pedro Montávez, Jose María López-Romero, Françoise Thais, Blanka Bartok, Ole Bøssing Christensen, Augustin Colette, Michel Déqué, et al. The impact of climate change on photovoltaic power generation in europe. *Nature communications*, 6(1):1–8, 2015.

[2] Govindasamy TamizhMani, Liang Ji, Yingtang Tang, Luis Petacci, and Carl Osterwald. Photovoltaic module thermal/wind performance: long-term monitoring and model development for energy rating. In *NCPV and Solar Program Review Meeting Proceedings, 24-26 March 2003, Denver, Colorado (CD-ROM)*, number NREL/CP-520-35645. National Renewable Energy Lab., Golden, CO.(US), 2003.

[3] Kristopher B Karnauskas, Julie K Lundquist, and Lei Zhang. Southward shift of the global wind energy resource under high carbon dioxide emissions. *Nature Geoscience*, 11(1):38–43, 2018.

[4] Nate Blair, Nicholas Diorio, Janine Freeman, Paul Gilman, Steven Janzou, Ty Neises, and Michael Wagner. System advisor model (sam) general description (version 2017.9. 5). *National Renewable Energy Laboratory Technical Report*, 2018.

[5] David Bolton. The computation of equivalent potential temperature. *Monthly weather review*, 108(7):1046–1053, 1980.

[6] Lee M Miller and David W Keith. Observation-based solar and wind power capacity factors and power densities. *Environmental Research Letters*, 13(10):104008, 2018.

[7] EPA. U.S. Environmental Protection Agency 2020 National Electric Energy Data System (Version 6.0). Online, 2020.

[8] Bipartisan Policy Center. Form eia-860 detailed data with previous form data (eia-860a/860b). *Energy Information Administration, Washington, DC*, 2020.

[9] EIA. Carbon Dioxide Emissions Coefficients. Online, 2020.

[10] AEO. Annual Energy Outlook 2020. Online, 2020.

[11] Sertaç Akar, Philipp Beiter, Wesley Cole, David Feldman, Parthiv Kurup, Eric Lantz, Robert Margolis, Debo Oladosu, Tyler Stehly, Gregory Rhodes, et al. 2020 annual technology baseline (atb) cost and performance data for electricity generation technologies. Technical report, National Renewable Energy Laboratory-Data (NREL-DATA), Golden, CO (United …, 2020.

[12] NREL. ReEDS OpenAccess. github, 2020.

[13] WECC. Western assessment of resource adequacy, Nov 2022.

[14] Jesse D Jenkins and Nestor A Sepulveda. Enhanced decision support for a changing electricity landscape: the genx configurable electricity resource capacity expansion model. 2017.

[15] Cassandra DW Rogers, Kai Kornhuber, Sarah E Perkins-Kirkpatrick, Paul C Loikith, and Deepti Singh. Sixfold increase in historical northern hemisphere concurrent large heatwaves driven by warming and changing atmospheric circulations. *Journal of Climate*, 35(3):1063–1078, 2022.